AIAA JOURNAL
Vol. 51, No. 3, March 2013

Transverse Waves in Simulated Liquid Rocket Engines

Charles T. Haddad* and Joseph Majdalani†
University of Tennessee Space Institute, Tullahoma, Tennessee 37388

DOI: 10.2514/1.J051912

This work seeks to provide a closed-form analytical solution for the transverse vorticoacoustic wave in a circular cylinder with headwall injection. This particular configuration mimics the conditions leading to the onset of traveling radial and tangential waves in an idealized liquid rocket engine. Assuming a short cylindrical chamber with two injection showerhead models (a top hat, uniform flow, and a bell-shaped sinusoidal profile), regular perturbations are used to linearize the problem's conservation equations. Flow decomposition is subsequently applied to the first-order disturbance equations, thus giving rise to a compressible, inviscid, acoustic set that is responsible for driving the unsteady motion, and to an incompressible, viscous, vortical set that is driven by virtue of coupling with the acoustic mode along solid boundaries. While the acoustic mode is readily recovered from the wave equation, the induced vortical mode is resolved using boundary-layer theory and a judicious expansion of the rotational equations with respect to a small viscous parameter, δ. After some effort, an explicit formulation is arrived at for each of the uniform and bell-shaped injection profiles. The two solutions are then presented, verified numerically, and compared at fixed spatial locations within the chamber. The penetration depth of the unsteady boundary layer is also characterized. Unlike the solution based on uniform headwall injection, the vorticoacoustic wave based on the bell-shaped mean flow is found to be more realistic; being capable of securing the no-slip requirement at both headwall and sidewall boundaries.

Nomenclature

a_0	=	speed of sound of incoming flow, $(\gamma R T_0)^{1/2}$
$\boldsymbol{e}_r$, $\boldsymbol{e}_\theta$, $\boldsymbol{e}_z$	=	unit vectors in r, θ, and z directions
L	=	chamber length
M_b	=	average blowing/burning Mach number at headwall
OF	=	overshoot factor
Pr	=	Prandtl number, ratio of kinematic viscosity to thermal diffusivity
p	=	pressure
R	=	chamber radius
Re_a	=	acoustic Reynolds number, $(a_0 R)/\nu_0$
Re_b	=	blowing Reynolds number at the headwall, $(U_b R)/\nu_0$
r, θ, z	=	radial, tangential, and axial coordinates
S	=	Strouhal number, $k_{mn}/M_b = (\omega_0 R)/U_b$
S_p	=	effective penetration number
T	=	temperature
t	=	time
$\boldsymbol{U}$	=	mean flow velocity vector
$U_b(r)$	=	blowing velocity profile at the headwall
$\boldsymbol{u}$	=	total velocity vector
V_w	=	propagation velocity of vortical waves in the axial direction
y_p, z_p	=	penetration depth of rotational elements in the y and z directions, respectively
z_{OS}	=	locus of unsteady velocity overshoot

Greek

γ	=	ratio of specific heats
δ	=	viscous parameter, $(Re_a)^{-1/2}$
δ_d	=	dilatational parameter, $\delta\sqrt{\eta_0/\mu_0 + 4/3}$
ε	=	wave amplitude
η	=	bulk viscosity
λ	=	spatial wave length
μ	=	dynamic viscosity
ν	=	kinematic viscosity, μ/ρ
ρ	=	density
$\boldsymbol{\Omega}$	=	mean vorticity
$\boldsymbol{\omega}$	=	unsteady vorticity
ω_0	=	nondimensional circular frequency

Subscripts

0	=	mean chamber properties

Superscripts

$*$	=	dimensional variables
$'$	=	unsteady flow variable
$-$	=	steady flow variable

I. Introduction

ACOUSTIC instability has long been recognized as one of the fundamental technical challenges plaguing large-scale combustors. Its preponderance in the developmental stages of international programs, such as Ares or Ariane has clearly positioned it as one of the chief obstacles that have historically hampered or delayed the deployment of new rocket launch systems. Although instabilities have been reported as early as the late 1930s, numerous studies of solid and liquid rockets have aimed at quantifying its sources. These have traditionally encompassed all three methods of investigations, namely, those based on experimental [1–4], numerical [5–8], and analytical thrusts [9–13].

In liquid rocket engines, transverse instabilities are identified by large pressure oscillations that occur in a plane perpendicular to the axis of the chamber and by frequencies that closely match the modes predicted through linear chamber acoustics [14,15]. Experimental

Presented as Paper 2011-6029 at the 47th AIAA/ASME/SAE/ASEE Joint Propulsion Conference & Exhibit, San Diego, CA, 31 –3 August 2011; received 21 February 2012; revision received 18 June 2012; accepted for publication 19 June 2012; published online 23 November 2012.

*Graduate Research Assistant, Department of Mechanical, Aerospace and Biomedical Engineering. Member AIAA.

†H. H. Arnold Chair of Excellence in Advanced Propulsion, Department of Mechanical, Aerospace and Biomedical Engineering. Associate Fellow AIAA.

observations have often suggested that instabilities entail large amplitude oscillations with steep gradients in the direction of the flow. In this vein, Clayton [2], Clayton et al. [3], and Sotter et al. [4] investigated high-amplitude tangential oscillations using a heavily instrumented, laboratory-scale, 20 klbf thrust engine. They recorded steep-fronted pressure oscillations with peak-to-peak amplitudes that were one order of magnitude larger than the mean chamber pressure. Although the response rate of their pressure transducers was not sufficiently high to capture the resulting wave character, their acquired data displayed large amplitude spikes followed by long and shallow pressure segments.

Along similar lines, several numerical studies have focused on the characterization of transverse waves and their effects on acoustic resonance in different rocket configurations. By way of example, Ando et al. [6] simulated the generation of transverse waves in a pulse detonation engine and deduced that the strength of the blasts increased where transverse waves collided. Other researchers, such as Chandrasekhar and Chakravarthy [7], deduced from their simulations that transverse waves could be induced by wall vibrations to the extent of producing longitudinal oscillations.

The earliest analytical studies of oscillatory waves in a ducted environment with injecting walls were undertaken by Culick [10,11], Hart and McClure [16,17], and others [18–21]. Their evolving models led to several analytical approximations that could be used to describe the behavior of oscillatory flows inside porous chambers. Other researchers employed asymptotic theory to linearize the Navier-Stokes equations and deduce the predicted wave behavior. This effort was prompted by the long-standing belief that the presence of a tangential acoustic velocity can give rise to a traveling shear wave. In 1956, theoretical work by Maslen and Moore [12] suggested that tangential waves could not steepen as in the case of longitudinal waves. However, their study of tangential wave development focused on a circular cylinder with no mean flow motion. In 1962, Crocco et al. [13] used small perturbations and separation of variables to predict the stability limit of liquid rocket engines. Their work showed that rocket stability depended on the radial and tangential modes, as well as the chamber's exit Mach number. Later studies [22] took into account the effects of the mean flow on wave growth and propagation in a cylinder with transpiring walls, this being the traditional geometry used to simulate a solid rocket motor.

Several studies followed and these have emphasized the need to observe the no-slip requirement at the propellant surface while pursuing viscous and rotational corrections to the acoustic field in a solid rocket motor (SRM). On one hand, Brown, Dunlap and collaborators [23,24] provided experimental data that confirmed the behavior of longitudinal oscillations in a simulated cold-flow chamber. Their results showed that irrotational models failed to satisfy the actual behavior directly above the propellant surface. On the other hand, Vuillot and Avalon [8] modeled the growth of the sidewall boundary layer using computational fluid dynamics. Their simulations predicted a thick Stokes layer at the sidewall, specifically one that could extend over the majority of the chamber volume for specific values of the control parameters. Subsequent investigations based on asymptotic tools led to closed-form approximations to this problem. It was found that the vorticoacoustic waves and their penetration within a rocket chamber strongly depended on the chamber acoustics along with the internal mean flow [18,25–27]. Some of the ensuing formulations confirmed the connection between the so-called penetration depth (i.e., rotational boundary layer), and the penetration number. This keystone parameter combined the injection Reynolds and Strouhal numbers in a nonintuitive way.

Retrospectively, most of these studies have been primarily concerned with the low-frequency oscillations arising in long solid rocket motors [28]. Conversely, much fewer models have been devoted to the liquid rocket engine (LRE) case [12,13,29]. For example, prompted by the need to better understand the mechanism of acoustic streaming, recent work by [21] has considered the transverse wave propagation problem in thrust chambers. Albeit, a secondary objective of theirs, these researchers have also tackled the vorticoacoustic boundary layer that forms in the vicinity of the injector faceplate. Their configuration may be viewed as somewhat analogous to a solid rocket motor in which the sidewall is exchanged for the headwall of a short LRE chamber.

In this article, we consider the unsteady flowfield in a short cylindrical chamber with a porous headwall that permits the injection of two specific mean flow patterns: uniform and bell shaped. In addition to the mean flow, the presence of small-amplitude oscillatory waves will be assumed. These self-excited waves give rise to a complex fluid structure that we wish to explore. Following the small perturbation approach introduced by Chu and Kovásznay [30], the equations of motion will be recast into two sets: one controlling the mean flow behavior, and the other describing the oscillatory motion. Then, using the Helmholtz decomposition theorem, the first-order fluctuations will be separated into a pair of acoustic and vortical fields. Presently, these techniques will be used to derive an improved asymptotic solution for the oscillatory motion in a circular chamber in general and a simulated LRE in particular. Using a systematic application of boundary-layer theory, an alternate mathematical formulation will be achieved and compared to previous work on the subject [21]. In so doing, the vorticoacoustic wave approximation based on the bell-shaped injection profile will be shown to provide an improved physical representation of the wave motion in a simulated thrust chamber.

II. Formulation

A. Geometry

As shown schematically in Fig. 1, the idealized thrust chamber is simulated as a circular cylinder that extends horizontally from the center axis at $r^* = 0$ to the sidewall at $r^* = R$. Vertically, the domain extends from $z* = 0$ to L, and the headwall may be viewed as a porous surface where the gases may be injected at a velocity $U_b(r)$. We also show in Fig. 1 the azimuthal coordinate, θ, and the transverse direction of unsteady velocity disturbances, u'_θ and u'_r, which denote both tangential and radial oscillations. Given that this study is focused on a simulated LRE, the aspect ratio of the chamber under consideration is taken to be small, specifically less than or equal to unity, $L/R \leq 1$.

B. Normalized System of Equations

It is helpful to first proceed by normalizing the flow variables according to

$$\begin{cases} p = p^*/P_0 & \boldsymbol{u} = \boldsymbol{u}^*/a_0 & r = r^*/R & T = T^*/T_0 \\ \rho = \rho^*/\rho_0 & t = t^*/(R/a_0) & z = z^*/R & \boldsymbol{\omega} = \boldsymbol{\omega}^*/(a_0/R) \end{cases} \tag{1}$$

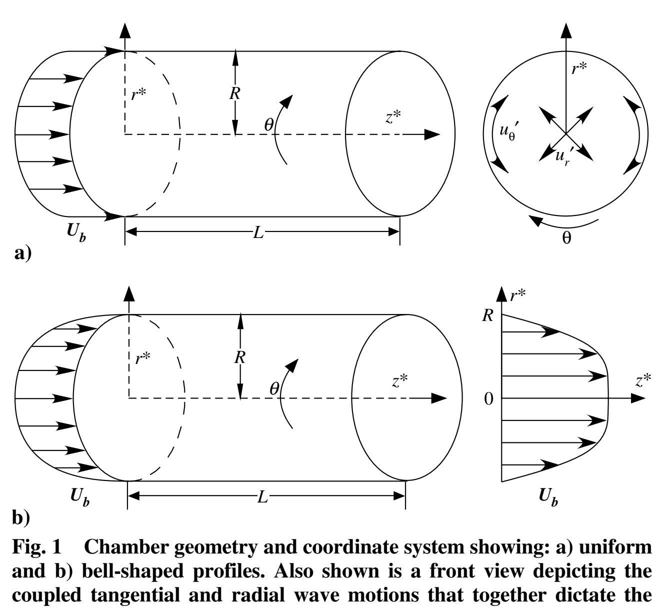

Fig. 1 Chamber geometry and coordinate system showing: a) uniform and b) bell-shaped profiles. Also shown is a front view depicting the coupled tangential and radial wave motions that together dictate the transverse mode shapes.

where reference properties are defined in the Nomenclature. The normalized governing equations for a viscous compressible fluid with no body forces acting on it may be expressed as

$$\text{Mass:}\qquad \frac{\partial \rho}{\partial t} + \nabla \cdot (\rho \boldsymbol{u}) = 0 \tag{2}$$

$$\text{Momentum:}\qquad \rho\left[\frac{\partial \boldsymbol{u}}{\partial t} + \frac{1}{2}\nabla(\boldsymbol{u}\cdot\boldsymbol{u}) - \boldsymbol{u}\times\nabla\times\boldsymbol{u}\right] = -\frac{1}{\gamma}\nabla p - \delta^2\nabla\times(\nabla\times\boldsymbol{u}) + \delta_d^2\nabla(\nabla\cdot\boldsymbol{u}) \tag{3}$$

$$\text{Energy:}\qquad \rho\left(\frac{\partial T}{\partial t} + \boldsymbol{u}\cdot\nabla T\right) = \frac{\gamma-1}{\gamma}\left(\frac{\partial p}{\partial t} + \boldsymbol{u}\cdot\nabla p\right) + \frac{\delta^2}{pr}\nabla^2 T \tag{4}$$

$$\text{State:}\qquad p = \rho T \tag{5}$$

where Pr and γ represent the Prandl number and the ratio of specific heats. The viscous parameters δ and δ_d are given by

$$\delta = \sqrt{\frac{\nu_0}{a_0 R}} = \frac{1}{\sqrt{Re_a}}; \qquad \delta_d = \delta\sqrt{\frac{\eta_0}{\mu_0} + \frac{4}{3}} \tag{6}$$

The bulk viscosity, also known as the dilatational viscosity η, is taken here at the reference conditions as η_0. It represents viscous shear associated with the volumetric-rate-of-strain; according to the Stokes hypothesis this parameter may be neglected when dealing with predominantly incompressible fluids.

C. Unsteady Disturbance Equations

As shown by Chu and Kovásznay [30], the normalized flow variables can be decomposed in terms of a mean flow and an oscillatory component viz:

$$\boldsymbol{u} = M_b\boldsymbol{U} + \boldsymbol{u}'; \qquad \boldsymbol{\omega} = \boldsymbol{\Omega} + \boldsymbol{\omega}'; \qquad p = 1 + p'; \qquad T = 1 + T' \tag{7}$$

Substituting the instantaneous variables of Eq. (7) into Eqs. (2)–(5) leads to two sets of equations for the steady and unsteady motions [18,25]. The next step is to expand all unsteady variables in terms of the primary perturbation parameter, ε. Each fluctuation a' may hence be written as

$$a' = \varepsilon a^{(1)} + \varepsilon^2 a^{(2)} + \varepsilon^3 a^{(3)} + \mathcal{O}(\varepsilon^4) \tag{8}$$

Here a alludes to a generic flow variable, and ε denotes the ratio of the superimposed oscillatory pressure amplitude to the traditionally larger mean chamber pressure. After some algebra, the governing equations may be separated at first order in ε and rearranged as

$$\begin{cases} \frac{\partial \rho^{(1)}}{\partial t} = -\nabla\cdot\boldsymbol{u}^{(1)} - M_b\nabla\cdot[\rho^{(1)}\boldsymbol{U}] \\ \frac{\partial \boldsymbol{u}^{(1)}}{\partial t} = -\frac{1}{\gamma}\nabla p^{(1)} - M_b\{\nabla[\boldsymbol{U}\cdot\boldsymbol{u}^{(1)}] - \boldsymbol{U}\times\boldsymbol{\omega}^{(1)} - \boldsymbol{u}^{(1)}\times\boldsymbol{\Omega}\} - \delta^2\nabla\times\boldsymbol{\omega}^{(1)} + \delta_d^2\nabla[\nabla\cdot\boldsymbol{u}^{(1)}] \\ \frac{\partial T^{(1)}}{\partial} = -M_b\boldsymbol{U}\cdot\nabla T^{(1)} + \frac{\gamma-1}{\gamma}\left[\frac{\partial p^{(1)}}{\partial t} + M_b\boldsymbol{U}\cdot\nabla p^{(1)}\right] + \frac{\delta^2}{Pr}\nabla^2 T^{(1)} \\ p^{(1)} = T^{(1)} + \rho^{(1)} \end{cases} \tag{9}$$

Equation (9) is often referred to as the set of interaction equations in which the influence of the mean flowfield, $\boldsymbol{U}$ on the unsteady disturbances, $\boldsymbol{u}^{(1)}$ is clearly seen.

D. Headwall Injection Pattern

It may be instructive to note that the system of first-order interaction equations encapsulated above is strongly dependent on $\boldsymbol{U}$, the steady stream of incoming fluid across the headwall. In practice, the injection process at the faceplate can be somewhat complex, specifically when taking into account the multitude of possible injector configurations and showerhead patterns. Nonetheless, it is routinely assumed that a streamtube motion quickly develops, especially for conventional thrust chambers [31]. Bearing these factors in mind, only low-order representations of the incoming jet will be considered here. In the interest of simplicity, two types of injections will be employed. The first corresponds to a uniform, top hat, plug flow along the chamber length, and the second implements a self-similar, bell-shaped, half-cosine that is often attributed to Berman [32]. The latter has been frequently used in theoretical studies of propulsive systems with headwall injection. Examples abound and one may cite, for example: Culick [22], Brown et al. [23], Proudman [33], Beddini [34], Chedevergne et al. [35], Griffond and Casalis [36], Saad and Majdalani [37], and Majdalani [38]. The two test cases may be represented in nondimensional form using

$$\text{Uniform profile:}\qquad \boldsymbol{U} = \boldsymbol{e}_z \tag{10}$$

$$\text{Berman (bell-shaped) profile:}\qquad \boldsymbol{U} = \cos\left(\tfrac{1}{2}\pi r^2\right)\boldsymbol{e}_z \tag{11}$$

In what follows, the vorticoacoustic transverse wave will be modeled in the presence of an oscillatory pressure disturbance and a mean flowfield corresponding to Eqs. (10) and (11).

E. Flowfield Decomposition

In comparable studies leading to analytical solutions of wave motions, the first-order fluctuations are invariably separated into an acoustic and a vortical field [39,40]. On the one hand, the acoustic part produces a potential motion that is compressible, irrotational, inviscid, and isentropic. On the other hand, the vortical part gives rise to an incompressible, rotational, and viscous field [27]. At the onset, the potential solution, being inviscid, proves incapable of satisfying the velocity adherence condition along solid boundaries. Both physically and mathematically, a correction is required, namely in the form of a vortical wave. The latter is generated at the boundary in such a manner as to offset the acoustic part at the wall. Using a circumflex to denote the pressure-driven potential part, and a tilde for the boundary-driven vortical component, the unsteady variables may be once more decomposed into

$$\boldsymbol{u}^{(1)} = \hat{\boldsymbol{u}} + \tilde{\boldsymbol{u}}; \qquad \boldsymbol{\omega}^{(1)} = \hat{\boldsymbol{\omega}} + \tilde{\boldsymbol{\omega}}; \qquad p^{(1)} = \hat{p} + \tilde{p}; \qquad \rho^{(1)} = \hat{\rho} + \tilde{\rho}; \qquad T^{(1)} = \hat{T} + \tilde{T} \tag{12}$$

Substituting Eq. (12) into Eq. (9) yields two independent sets of equations that remain coupled by virtue of the no-slip requirement at the headwall [40]. These are

$$\text{Acoustic set:}\begin{cases}\frac{\partial\hat{\rho}}{\partial t}=-\nabla\cdot\hat{\boldsymbol{u}}-M_b\boldsymbol{U}\nabla\cdot\hat{\rho}; \qquad \frac{\partial\hat{\boldsymbol{u}}}{\partial t}=-\frac{1}{\gamma}\nabla\hat{p}-M_b[\nabla(\boldsymbol{U}\cdot\hat{\boldsymbol{u}})-\hat{\boldsymbol{u}}\times\boldsymbol{\Omega}]\\ \frac{\partial\hat{T}}{\partial t}=-M_b\boldsymbol{U}\cdot\nabla\hat{T}+\frac{\gamma-1}{\gamma}\left(\frac{\partial\hat{p}}{\partial t}+M_b\boldsymbol{U}\cdot\nabla\hat{p}\right)\\ \hat{p}=\hat{T}+\hat{\rho}; \qquad \hat{\rho}=\gamma\hat{\rho}\end{cases} \tag{13}$$

$$\text{Vortical set:}\begin{cases}\nabla\cdot\tilde{\boldsymbol{u}}=0; \qquad \frac{\partial\tilde{\boldsymbol{u}}}{\partial t}=-\frac{1}{\gamma}\nabla\tilde{p}-M_b[\nabla(\boldsymbol{U}\cdot\tilde{\boldsymbol{u}})-\boldsymbol{U}\times\tilde{\boldsymbol{\omega}}-\tilde{\boldsymbol{u}}\times\boldsymbol{\Omega}]-\delta^2\nabla\times\tilde{\boldsymbol{\omega}}+\delta_d^2\nabla(\nabla\cdot\tilde{\boldsymbol{u}})\\ \frac{\partial\tilde{T}}{\partial t}=-M_b\boldsymbol{U}\cdot\nabla\tilde{T}+\frac{\gamma-1}{\gamma}\left(\frac{\partial\tilde{p}}{\partial t}+M_b\boldsymbol{U}\cdot\nabla\tilde{p}\right)+\frac{\delta^2}{Pr}\nabla^2\tilde{T}\\ \tilde{p}=\tilde{T}+\tilde{\rho}\end{cases} \tag{14}$$

F. Boundary Conditions

The fundamental disparities between acoustic and vortical fields warrant the use of two dissimilar sets of boundary conditions. In the case of the acoustic wave, a closed boundary must be maintained, as usual, along all solid surfaces, including the injection site (i.e., at $r=1$, $z=0$ and $z=L/R$). In the case of the rotational wave, the no slip at the headwall must be secured first and foremost, being the counterpart of the sidewall boundary in the inverted analog of an axially traveling wave within an elongated porous cylinder [21,40]. In both geometric configurations, the velocity adherence constraint is imposed at the injecting surfaces, and these correspond to either the headwall or the sidewall of the simulated LRE and SRM, respectively. Along the noninjecting surface (sidewall), slip may be allowed in the vortical wave formulation. At the downstream end of the chamber, $z=L/R$, the vortical wave must remain bounded and, being sufficiently removed from the headwall, its rotational effects are expected to have died out. Naturally, with the attenuation of the unsteady vorticity component, the wave reduces to its potential form. A summary of the physical constraints entailed in the resulting model is given in Table 1.

III. Solution

This section describes the boundary-layer approach that we follow to reduce the time-dependent vortical system into a more manageable set. The ensuing formulations are provided for both mean flow profiles. However, because the vortical field is engendered by the acoustic wave, the latter must be considered first.

A. Acoustic Formulation

Although Eq. (13) consists of an assortment of five equations, it can be systematically reduced to a single equation that represents a modified form of the wave equation. Using a well-established manipulation of the acoustic set, the time derivative of the acoustic mass conservation may be subtracted from the divergence of the momentum equation to arrive at an extended form of the wave equation [21], namely

$$\frac{\partial^2\hat{p}}{\partial t^2}=\nabla^2\hat{p}+M_b\left[\gamma\nabla^2(\boldsymbol{U}\cdot\hat{\boldsymbol{u}})-\gamma\nabla\cdot(\hat{\boldsymbol{u}}\times\boldsymbol{\Omega})-\frac{\partial}{\partial t}(\boldsymbol{U}\nabla\cdot\hat{p})\right] \tag{15}$$

Note that Eq. (15) incorporates the effects of the mean flow, albeit, at the order of the blowing Mach number. At this juncture, it may be useful to recall that the inlet or blowing Mach number is usually smaller than unity ($M_b\le 0.3$). As such, it may be used as a secondary perturbation parameter. This enables us to expand the acoustic pressure in successive powers of M_b, viz

$$\hat{p}=\hat{p}^{(0)}+M_b\hat{p}^{(1)}+M_b^2\hat{p}^{(2)}+\mathcal{O}(M_b^3) \tag{16}$$

Forthwith, backward substitution into Eq. (15) renders, at leading order

$$\frac{\partial^2\hat{p}^{(0)}}{\partial t^2}=\nabla^2\hat{p}^{(0)} \tag{17}$$

As usual, we recover the classical wave equation in three dimensions. The solution of this partial differential equation (PDE) may be readily extracted using the separation of variables. One gets

$$\hat{p}^{(0)}(t,r,\theta,z)=e^{-ik_lt}J_m(k_{mn}r)\cos(m\theta)\cos(k_lz) \tag{18}$$

where t, m, n and l are positive integers that refer to the temporal, tangential, radial, and longitudinal mode numbers, respectively. In the same vein, k_{mn} designates the transverse wave number that depends on the joint tangential and radial modes, m and n. In practice, it may be deduced numerically by solving $J_m'(k_{mn})=0$ and generating, in successive fashion [21], the first radial, first tangential, first radial and tangential modes, etc., according to

$$\begin{cases}k_{01}\approx 3.83170597 & k_{10}\approx 1.84118378 & k_{11}\approx 5.33144277\\ k_{02}\approx 7.01558667 & k_{20}\approx 3.05423693 & k_{22}\approx 9.96946782\\ k_{12}\approx 8.53631637 & k_{21}\approx 6.70613319 & \text{etc.}\end{cases} \tag{19}$$

To simplify the forthcoming analysis, we note that for a short cylindrical enclosure in general, or a simulated LRE in particular, the tangential and radial oscillations tend to dominate over their longitudinal counterpart, mainly due to the short length of the chamber. Hence, in our effort to emphasize the contribution of the transverse modes, and given that $\cos(k_lz)$ remains close to unity for small z, one may set $k_l\approx 0$ and reduce the leading-order acoustic pressure into

$$\hat{p}^{(0)}(t,r,\theta,z)=e^{-ik_{mn}t}J_m(k_{mn}r)\cos(m\theta) \tag{20}$$

The corresponding acoustic velocity may be deduced by integrating the momentum equation and evaluating

$$\hat{\boldsymbol{u}}^{(0)}=-\frac{1}{\gamma}\int\nabla\hat{p}^{(0)}\,\mathrm{d}t \tag{21}$$

As such, a complete leading-order acoustic solution is realized, specifically

$$\begin{cases}\hat{p}=e^{-ik_{mn}t}J_m(k_{mn}r)\cos(m\theta); \qquad \hat{u}_r=-\frac{i}{k_{mn}\gamma}e^{-ik_{mn}t}J_m'(k_{mn}r)\cos(m\theta)\\ \hat{u}_\theta=\frac{i}{k_{mn}\gamma}\frac{m}{r}e^{-ik_{mn}t}J_m(k_{mn}r)\sin(m\theta); \qquad \hat{u}_z=0\end{cases} \tag{22}$$

Table 1 Boundary conditions for the acoustic and vortical fields

	Boundary		
	$r=1$	$z=0$	$z=L/R$
Acoustic field	$\mathbf{n}\cdot\nabla\hat{p}=0$	$\mathbf{n}\cdot\nabla\hat{p}=0$	$\mathbf{n}\cdot\nabla\hat{p}=0$
Vortical field	No condition imposed	$u_r'=u_\theta'=u_z'=0$	Bounded

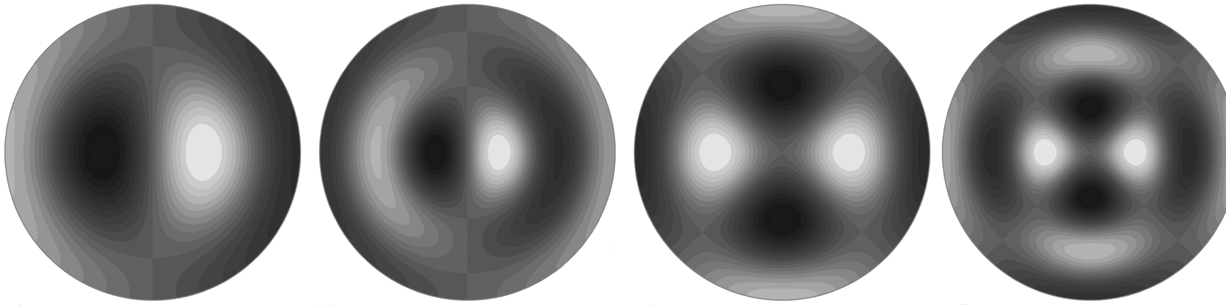

a) b) c) d)

Fig. 2 Pressure contours in a polar slice for transverse oscillations corresponding to: a) $k_{11} = 5.3314$, b) $k_{12} = 8.5363$, c) $k_{21} = 6.7061$, and d) $k_{22} = 9.9695$.

In Eq. (22) and what follows, a prime will be used to denote the differentiation with respect to the radial coordinate.

For the reader's convenience, the four parts of Fig. 2 are produced to illustrate the instantaneous pressure distribution in a cylindrical chamber at four sequential mode numbers. These correspond to four zeroes of J'_m that are enumerated in Eq. (19). Everywhere, the pressure contours represent snapshots taken in a polar plane at $t = 0.01$ s, $\forall z$, where darker and lighter shades denote higher and lower values, respectively. It is interesting to note the evolution of the nodal lines going from a) to d), thus giving rise to double-D and alternating cross patterns that characterize the acoustic modes shapes. In a) and b), the first and second radial modes are featured along with the first tangential mode where alternating double-D contours appear either a) once or b) twice, with the second set brushing along the outer periphery. In c) and d), the second tangential configuration is depicted at the first and second radial modes. The last contour clearly captures the symmetrically alternating wave structure in both tangential and radial directions.

B. Vortical Formulation

Before proceeding with the solution of the vortical disturbance, it may be useful to clarify the origin of the driving mechanisms for the waves in question, while paying special attention to the reason for the decoupling of the incompressible continuity and momentum equations from the remaining members in Eq. (14). To this end, we recall that the acoustic wave is induced by the pressure differential in the chamber, but remains uninfluenced by the no-slip requirement at the boundaries or the mean flow at the leading order in M_b. In contrast, the vortical waves are entirely driven by the acoustic motion at the boundaries and appear only as a dissipating correction that is impacted by the chamber's geometry, the mean flow, and the acoustic field. It may hence be argued that the rotational pressure contribution may be dismissed in view of the pressure differential being mainly prescribed by the acoustic field. This assumption enables us to ignore $\tilde{p}$ as a first-cut approximation in the reduced momentum equation [18], which simplifies the remaining set into

$$\begin{cases} \nabla\cdot\tilde{\boldsymbol{u}} = 0 \\ \frac{\partial\tilde{\boldsymbol{u}}}{\partial t} = -M_b[\nabla(\boldsymbol{U}\cdot\tilde{\boldsymbol{u}}) - \boldsymbol{U}\times\tilde{\boldsymbol{\omega}} - \tilde{\boldsymbol{u}}\times\boldsymbol{\Omega}] - \delta^2\nabla\times\tilde{\boldsymbol{\omega}} \end{cases} \tag{23}$$

Interestingly, the system in Eq. (23) becomes overdetermined, being comprised of four equations with three unknowns: the three velocity components, $\tilde{u}_r$, $\tilde{u}_\theta$, and $\tilde{u}_z$. A solution based on any three equations has the propensity to generate a large error in the fourth equation, depending on which three are chosen. To mathematically close the system, one can retain the small vortical pressure wave $\tilde{p}$ in the momentum equation. The amended set becomes

$$\begin{cases} \nabla\cdot\tilde{\boldsymbol{u}} = 0 \\ \frac{\partial\tilde{\boldsymbol{u}}}{\partial t} = -\frac{1}{\gamma}\nabla\tilde{p} - M_b[\nabla(\boldsymbol{U}\cdot\tilde{u}) - \boldsymbol{U}\times\tilde{\boldsymbol{\omega}} - \tilde{\boldsymbol{u}}\times\boldsymbol{\Omega}] - \delta^2\nabla\times\tilde{\boldsymbol{\omega}} \end{cases} \tag{24}$$

In seeking an ansatz for $\tilde{\boldsymbol{u}}$, we note that, in Eq. (24), the rotational velocity disturbance stands as a function of time and three spatial variables. Moreover, $\tilde{\boldsymbol{u}}(t, r, \theta, z)$ must be chosen in a manner to identically cancel the acoustic motion at the headwall, $\forall t$. The time dependence of the vortical field must, therefore, match that of the acoustic motion at the headwall. This can be achieved when the unsteady vortical wave exhibits the form

$$\tilde{\boldsymbol{u}} = e^{-ik_{mn}t}f(r,\theta,z) \quad \text{or} \quad \frac{\partial\tilde{\boldsymbol{u}}}{\partial t} = -ik_{mn}e^{-ik_{mn}t}f(r,\theta,z) = -ik_{mn}\tilde{\boldsymbol{u}} \tag{25}$$

This ansatz will be later used to secure a closed-form vortical approximation.

C. Uniform Mean Flow

The transverse wave subject to a uniform mean flow is briefly explored by [21], particularly, in the investigation of the acoustic streaming mechanism in a simulated LRE. The present extension begins by applying a regular perturbation expansion to a well-established variant of the conservation equations. For the case of a uniform mean flow, Eq. (24) may be expanded in scalar notation to produce

$$\begin{cases} \frac{\tilde{u}_r}{r} + \frac{\partial\tilde{u}_r}{\partial r} + \frac{1}{r}\frac{\partial\tilde{u}_\theta}{\partial\theta} + \frac{\partial\tilde{u}_z}{\partial z} = 0 \\ -ik_{mn}\tilde{u}_r + M_b\frac{\partial\tilde{u}_r}{\partial z} = \frac{1}{\gamma}\frac{\partial\tilde{p}}{\partial r} + \delta^2\left(\frac{\partial^2\tilde{u}_r}{\partial z^2} + \frac{1}{r^2}\frac{\partial^2\tilde{u}_r}{\partial\theta^2} - \frac{1}{r^2}\frac{\partial\tilde{u}_\theta}{\partial\theta} - \frac{1}{r}\frac{\partial^2\tilde{u}_\theta}{\partial r\partial\theta} - \frac{\partial^2\tilde{u}_z}{\partial r\partial z}\right) \\ -ik_{mn}\tilde{u}_\theta + M_b\frac{\partial\tilde{u}_\theta}{\partial z} = -\frac{1}{\gamma r}\frac{\partial\tilde{p}}{\partial\theta} + \delta^2\left(\frac{1}{r^2}\frac{\partial\tilde{u}_r}{\partial\theta} - \frac{1}{r}\frac{\partial^2\tilde{u}_r}{\partial r\partial\theta} - \frac{\tilde{u}_\theta}{r^2} + \frac{\partial^2\tilde{u}_\theta}{\partial z^2} + \frac{1}{r}\frac{\partial\tilde{u}_\theta}{\partial r} + \frac{\partial^2\tilde{u}_\theta}{\partial r^2} - \frac{1}{r}\frac{\partial^2\tilde{u}_z}{\partial\theta\partial z}\right) \\ -ik_{mn}\tilde{u}_z + M_b\frac{\partial\tilde{u}_z}{\partial z} = -\frac{1}{\gamma}\frac{\partial\tilde{p}}{\partial z} - \delta^2\left(\frac{1}{r}\frac{\partial\tilde{u}_r}{\partial z} + \frac{\partial^2\tilde{u}_r}{\partial r\partial z} + \frac{1}{r}\frac{\partial^2\tilde{u}_\theta}{\partial\theta\partial z} - \frac{1}{r^2}\frac{\partial^2\tilde{u}_z}{\partial\theta^2} - \frac{1}{r}\frac{\partial\tilde{u}_z}{\partial r} - \frac{\partial^2\tilde{u}_z}{\partial r^2}\right) \end{cases} \tag{26}$$

Recognizing that the vortical wave is dominant near the boundaries, Eq. (26) may be transformed using boundary-layer theory, with the no-slip boundary condition being enforced at the headwall. Because the vortical wave can grow or decay in the axial direction, we rescale the axial variable using a stretched inner coordinate

$$\zeta = \frac{z}{\delta} \tag{27}$$

The next step is to perturb the vortical variables that appear in Eq. (26) with respect to the viscous parameter using

$$\tilde{a} = \tilde{a}^{(0)} + \delta\tilde{a}^{(1)} + \delta^2\tilde{a}^{(2)} + \delta^3\tilde{a}^{(3)} + \mathcal{O}(\delta^4) \tag{28}$$

Collecting the terms of the same order in δ and rearranging leads to two vortical sets that must be solved successively.

1. Leading-Order Solution

At $\mathcal{O}(1)$, Eq. (26) begets

$$\frac{\partial \tilde{u}_\zeta^{(0)}}{\partial \zeta} = 0 \tag{29}$$

$$-ik_{mn}\tilde{u}_r^{(0)} + \frac{M_b}{\delta}\frac{\partial \tilde{u}_r^{(0)}}{\partial \zeta} - \frac{\partial^2 \tilde{u}_r^{(0)}}{\partial \zeta^2} = -\frac{1}{\gamma}\frac{\partial \tilde{p}^{(0)}}{\partial r} \tag{30}$$

$$-ik_{mn}\tilde{u}_\theta^{(0)} + \frac{M_b}{\delta}\frac{\partial \tilde{u}_\theta^{(0)}}{\partial \zeta} - \frac{\partial^2 \tilde{u}_\theta^{(0)}}{\partial \zeta^2} = -\frac{1}{\gamma r}\frac{\partial \tilde{p}^{(0)}}{\partial \theta} \tag{31}$$

$$\frac{1}{\gamma}\frac{\partial \tilde{p}^{(0)}}{\partial \zeta} = 0 \tag{32}$$

From one perspective, solving Eq. (32) leads to an axially invariant $\tilde{p}^{(0)}$ that is only a function of the radial, tangential, and time variables. One confirms that the axial propagation of the vortical wave is driven solely by the no-slip condition at the headwall. At this order, the vortical pressure does not affect the wave generated and must be set equal to zero to preserve the physicality of the case at hand. Similarly, Eq. (29) leads to a vanishing leading-order axial velocity contribution. In short, we collect

$$\tilde{p}^{(0)} = 0; \qquad \tilde{u}_\zeta^{(0)} = 0 \tag{33}$$

From another perspective, the solutions of Eqs. (30) and (31) may be straightforwardly extracted. The radial, now homogeneous PDE precipitates

$$\tilde{u}_r^{(0)} = A_{r0}(t,r,\theta)e^{X_1\zeta} + B_{r0}(t,r,\theta)e^{X_2\zeta} \tag{34}$$

where

$$X_1 = \frac{M_b}{2\delta}\left(1 - \sqrt{1 - \frac{4ik_{mn}\delta^2}{M_b^2}}\right) = \frac{M_b}{2\delta}\left(1 - \sqrt{\frac{1}{2} + \frac{1}{2}\sqrt{1 + \frac{16k_{mn}^2\delta^4}{M_b^4}}} + i\sqrt{\frac{1}{2}\sqrt{1 + \frac{16k_{mn}^2\delta^4}{M_b^4}} - \frac{1}{2}}\right) \tag{35}$$

$$X_2 = \frac{M_b}{2\delta}\left(1 + \sqrt{1 - \frac{4ik_{mn}\delta^2}{M_b^2}}\right) = \frac{M_b}{2\delta}\left(1 + \sqrt{\frac{1}{2} + \frac{1}{2}\sqrt{1 + \frac{16k_{mn}^2\delta^4}{M_b^4}}} - i\sqrt{\frac{1}{2}\sqrt{1 + \frac{16k_{mn}^2\delta^4}{M_b^4}} - \frac{1}{2}}\right) \tag{36}$$

At this juncture, two physical constraints may be brought to bear: the physicality of the solution in the farfield and the no-slip requirement at the headwall. First, because the real part of X_2 remains positive, $B_{r0}(r,\theta,t)$ must be suppressed to prevent the unbounded, unphysical growth of the velocity as ζ tends to infinity. Equation (34) reduces to

$$\tilde{u}_r^{(0)} = A_{r0}(t,r,\theta)e^{X_1\zeta} \tag{37}$$

Second, the velocity adherence condition at the headwall ($\zeta = 0$) demands that

$$\tilde{u}_r^{(0)}(t,r,\theta,0) + \hat{u}_r(t,r,\theta,0) = 0 \tag{38}$$

and so

$$A_{r0}(t,r,\theta) = \frac{i}{k_{mn}\gamma}e^{-ik_{mn}t}\cos(m\theta)J_m'(k_{mn}r) \tag{39}$$

or

$$\tilde{u}_r^{(0)} = \frac{i}{k_{mn}\gamma}e^{-ik_{mn}t}e^{X_1\zeta}\cos(m\theta)J_m'(k_{mn}r) \tag{40}$$

A similar procedure can be used to solve Eq. (31) with the outcome being

$$\tilde{u}_\theta^{(0)} = -\frac{i}{k_{mn}\gamma}\frac{m}{r}e^{-ik_{mn}t}e^{X_1\zeta}\sin(m\theta)J_m(k_{mn}r) \tag{41}$$

2. First-Order Solution

At $\mathcal{O}(\delta)$, Eq. (26) yields

$$\frac{\partial \tilde{u}_\zeta^{(1)}}{\partial \zeta} = -\frac{1}{r}\tilde{u}_r^{(0)} - \frac{\partial \tilde{u}_r^{(0)}}{\partial r} - \frac{1}{r}\frac{\partial \tilde{u}_\theta^{(0)}}{\partial \theta} \tag{42}$$

$$ik_{mn}\tilde{u}_r^{(1)} - \frac{M_b}{\delta}\frac{\partial \tilde{u}_r^{(1)}}{\partial \zeta} + \frac{\partial^2 \tilde{u}_r^{(1)}}{\partial \zeta^2} = \frac{1}{\gamma}\frac{\partial \tilde{p}^{(1)}}{\partial r} + \frac{\partial^2 \tilde{u}_\zeta^{(0)}}{\partial r\partial \zeta} \tag{43}$$

$$ik_{mn}\tilde{u}_\theta^{(1)} - \frac{M_b}{\delta}\frac{\partial \tilde{u}_\theta^{(1)}}{\partial \zeta} + \frac{\partial^2 \tilde{u}_\theta^{(1)}}{\partial \zeta^2} = -\frac{1}{\gamma r}\frac{\partial \tilde{p}^{(1)}}{\partial \theta} + \frac{1}{r}\frac{\partial^2 \tilde{u}_\zeta^{(0)}}{\partial \theta\partial \zeta} \tag{44}$$

$$\frac{1}{\gamma}\frac{\partial \tilde{p}^{(1)}}{\partial \zeta} = ik_{mn}\tilde{u}_\zeta^{(0)} - \frac{M_b}{\delta}\frac{\partial \tilde{u}_\zeta^{(0)}}{\partial \zeta} \tag{45}$$

The vanishing leading-order axial velocity returns $\tilde{p}^{(1)} = 0$. Subsequently, Eq. (43) reduces to

$$ik_{mn}\tilde{u}_r^{(1)} - \frac{M_b}{\delta}\frac{\partial \tilde{u}_r^{(1)}}{\partial \zeta} + \frac{\partial^2 \tilde{u}_r^{(1)}}{\partial \zeta^2} = 0 \tag{46}$$

The solution of this homogenous PDE is analogous to that of Eq. (37), namely

$$\tilde{u}_r^{(1)} = A_{r1}(t,r,\theta)e^{X_1\zeta} \tag{47}$$

Here too, the no-slip condition must be fulfilled. However, since the cancellation of the acoustic velocity has been accomplished at the previous order, the leading-order contribution at the headwall must not interfere. This implies

$$\tilde{u}_r^{(1)}(t,r,\theta,0) = 0 \tag{48}$$

Equation (48) results in a vanishing first-order radial velocity. A parallel procedure applies to the tangential component in Eq. (44), which mirrors Eq. (43). We get

$$\tilde{u}_r^{(1)} = \tilde{u}_\theta^{(1)} = 0 \tag{49}$$

At this point, the axial component may be resolved. By substituting Eqs. (40) and (41) into Eq. (42), we obtain

$$\frac{\partial \tilde{u}_\zeta^{(1)}}{\partial \zeta} = \frac{ik_{mn}}{\gamma} e^{-ik_{mn}t} e^{X_1\zeta} \cos(m\theta) J_m(k_{mn}r) \tag{50}$$

Equation (50) may be integrated and made to satisfy the headwall boundary condition. This operation entails

$$\tilde{u}_\zeta^{(1)} = \frac{ik_{mn}}{\gamma} e^{-ik_{mn}t} \frac{e^{X_1\zeta}}{X_1} \cos(m\theta) J_m(k_{mn}r) + A_{\zeta 1}(t, r, \theta) \tag{51}$$

$$\text{and} \qquad \tilde{u}_\zeta^{(1)}(t, r, \theta, 0) = 0 \quad \text{or}$$

$$A_{\zeta 1}(t, r, \theta) = -\frac{ik_{mn}}{\gamma}\frac{1}{X_1} e^{-ik_{mn}t} \cos(m\theta) J_m(k_{mn}r) \tag{52}$$

$$\text{whence} \qquad \tilde{u}_\zeta^{(1)} = \frac{ik_{mn}}{\gamma}\frac{1}{X_1} e^{-ik_{mn}t} \cos(m\theta) J_m(k_{mn}r)(e^{X_1\zeta} - 1) \tag{53}$$

D. Bell-Shaped Mean Flow

It may be argued that the one-dimensional bell-shaped mean flow stands to provide a better physical approximation to the faceplate injection mechanism. While the uniform profile allows for slippage at the boundary, the bell-shaped motion overcomes this deficiency by forcing the fluid to vanish at the sidewall. Through the use of a more realistic representation of the mean flow, an improved solution for the transverse oscillations may hence be achieved. In this case, the expansion of Eq. (24) with respect to the mean flow in Eq. (11) produces

$$\frac{\tilde{u}_r}{r} + \frac{\partial \tilde{u}_r}{\partial r} + \frac{1}{r}\frac{\partial \tilde{u}_\theta}{\partial \theta} + \frac{\partial \tilde{u}_z}{\partial z} = 0 \tag{54}$$

$$-ik_{mn}\tilde{u}_r + M_b \cos\left(\tfrac{1}{2}\pi r^2\right)\frac{\partial \tilde{u}_r}{\partial z} = -\frac{1}{\gamma}\frac{\partial \tilde{p}}{\partial r} + \delta^2\left(\frac{\partial^2 \tilde{u}_r}{\partial z^2} + \frac{1}{r^2}\frac{\partial^2 \tilde{u}_r}{\partial \theta^2} - \frac{1}{r^2}\frac{\partial \tilde{u}_\theta}{\partial \theta} - \frac{1}{r}\frac{\partial^2 \tilde{u}_\theta}{\partial r \partial \theta} - \frac{\partial^2 \tilde{u}_z}{\partial r \partial z}\right) \tag{55}$$

$$-ik_{mn}\tilde{u}_\theta + M_b \cos\left(\tfrac{1}{2}\pi r^2\right)\frac{\partial \tilde{u}_\theta}{\partial z} = -\frac{1}{\gamma r}\frac{\partial \tilde{p}}{\partial \theta} + \delta^2\left(\frac{1}{r^2}\frac{\partial \tilde{u}_r}{\partial \theta} - \frac{1}{r}\frac{\partial^2 \tilde{u}_r}{\partial r \partial \theta} - \frac{\tilde{u}_\theta}{r^2} + \frac{\partial^2 \tilde{u}_\theta}{\partial z^2} + \frac{1}{r}\frac{\partial \tilde{u}_\theta}{\partial r} + \frac{\partial^2 \tilde{u}_\theta}{\partial r^2} - \frac{1}{r}\frac{\partial^2 \tilde{u}_z}{\partial \theta \partial z}\right) \tag{56}$$

$$-ik_{mn}\tilde{u}_z + M_b \cos\left(\tfrac{1}{2}\pi r^2\right)\frac{\partial \tilde{u}_z}{\partial z} - M_b \pi r \sin\left(\tfrac{1}{2}\pi r^2\right)\tilde{u}_r = -\frac{1}{\gamma}\frac{\partial \tilde{p}}{\partial z} + \delta^2\left(-\frac{1}{r}\frac{\partial \tilde{u}_r}{\partial z} - \frac{\partial^2 \tilde{u}_r}{\partial r \partial z} - \frac{1}{r}\frac{\partial^2 \tilde{u}_\theta}{\partial \theta \partial z} + \frac{1}{r^2}\frac{\partial^2 \tilde{u}_z}{\partial \theta^2} + \frac{1}{r}\frac{\partial \tilde{u}_z}{\partial r} + \frac{\partial^2 \tilde{u}_z}{\partial r^2}\right) \tag{57}$$

The next step is to invoke boundary-layer theory to stretch the axial coordinate and reduce Eqs. (54–57) asymptotically by perturbing the resulting set with respect to δ.

1. *Leading-Order Solution*

Using $\zeta = z/\delta$ and a series after Eq. (28), Eqs. (54–57) may be expanded and segregated at $\mathcal{O}(1)$ into

$$\frac{\partial \tilde{u}_\zeta^{(0)}}{\partial \zeta} = 0 \tag{58}$$

$$-ik_{mn}\tilde{u}_r^{(0)} + \frac{M_b}{\delta}\cos\left(\tfrac{1}{2}\pi r^2\right)\frac{\partial \tilde{u}_r^{(0)}}{\partial \zeta} - \frac{\partial^2 \tilde{u}_r^{(0)}}{\partial \zeta^2} = -\frac{1}{\gamma}\frac{\partial \tilde{p}^{(0)}}{\partial r} \tag{59}$$

$$-ik_{mn}\tilde{u}_\theta^{(0)} + \frac{M_b}{\delta}\cos\left(\tfrac{1}{2}\pi r^2\right)\frac{\partial \tilde{u}_\theta^{(0)}}{\partial \zeta} - \frac{\partial^2 \tilde{u}_\theta^{(0)}}{\partial \zeta^2} = -\frac{1}{\gamma r}\frac{\partial \tilde{p}^{(0)}}{\partial \theta} \tag{60}$$

$$\frac{1}{\gamma}\frac{\partial \tilde{p}^{(0)}}{\partial \zeta} = 0 \tag{61}$$

The treatment of Eqs. (61) then (58) mirrors the case of uniform injection. The leading-order pseudopressure and axial velocity are both determined to be vanishingly small, or $\tilde{p}^{(0)} = \tilde{u}_\zeta^{(0)} = 0$. However, the solution of Eq. (59) leaves us with

$$\tilde{u}_r^{(0)} = A_r(t, r, \theta)e^{X_{1c}\zeta} + B_r(t, r, \theta)e^{X_{2c}\zeta} \tag{62}$$

where

$$X_{1C}(r) = \frac{M_b}{2\delta}\cos\left(\frac{1}{2}\pi r^2\right)\left[1 - \sqrt{1 - \frac{4ik_{mn}\delta^2}{M_b^2\cos^2(\frac{1}{2}\pi r^2)}}\right] = \frac{M_b}{2\delta}\cos\left(\frac{1}{2}\pi r^2\right)\left[1 - \sqrt{\frac{1}{2} + \frac{1}{2}\sqrt{1 + \frac{16k_{mn}^2\delta^4}{M_b^4\cos^4(\frac{1}{2}\pi r^2)}}} + i\sqrt{\frac{1}{2}\sqrt{1 + \frac{16k_{mn}^2\delta^4}{M_b^4\cos^4(\frac{1}{2}\pi r^2)}} - \frac{1}{2}}\right] \tag{63}$$

$$X_{2C}(r) = \frac{M_b}{2\delta}\cos\left(\frac{1}{2}\pi r^2\right)\left[1 + \sqrt{1 - \frac{4ik_{mn}\delta^2}{M_b^2\cos^2(\frac{1}{2}\pi r^2)}}\right] = \frac{M_b}{2\delta}\cos\left(\frac{1}{2}\pi r^2\right)\left[1 + \sqrt{\frac{1}{2} + \frac{1}{2}\sqrt{1 + \frac{16k_{mn}^2\delta^4}{M_b^4\cos^4(\frac{1}{2}\pi r^2)}}} - i\sqrt{\frac{1}{2}\sqrt{1 + \frac{16k_{mn}^2\delta^4}{M_b^4\cos^4(\frac{1}{2}\pi r^2)}} - \frac{1}{2}}\right] \tag{64}$$

Because all cosine terms remain positive in the domain of interest, the real part of X_{2C} stays positive as well. One must set $B_r(t, r, \theta) = 0$ to mitigate the exponential growth of $\tilde{u}_r^{(0)}$ as $\zeta \to \infty$, a condition that materializes at the outer edge of the boundary layer. This implies

$$\tilde{u}_r^{(0)} = A_{r0}(t, r, \theta)e^{X_1\zeta} \tag{65}$$

Lastly, prevention of slippage at the headwall enables us to deduce $A_{r0}(t, r, \theta)$ and, therefore,

$$\tilde{u}_r^{(0)} = \frac{i}{k_{mn}\gamma} e^{-ik_{mn}t} e^{X_{1C}\zeta} \cos(m\theta) J_m'(k_{mn}r) \tag{66}$$

A nearly identical procedure leads to the identification of the tangential component, specifically

$$\tilde{u}_\theta^{(0)} = -\frac{i}{k_{mn}\gamma}\frac{m}{r} e^{-ik_{mn}t} e^{X_{1C}\zeta} \sin(m\theta) J_m(k_{mn}r) \tag{67}$$

2. First-Order Solution

The first-order expansion of Eqs. (54–57) precipitates

$$\frac{\partial \tilde{u}_\zeta^{(1)}}{\partial \zeta} = -\frac{1}{r}\tilde{u}_r^{(0)} - \frac{\partial \tilde{u}_r^{(0)}}{\partial r} - \frac{1}{r}\frac{\partial \tilde{u}_\theta^{(0)}}{\partial \theta} \tag{68}$$

$$ik_{mn}\tilde{u}_r^{(1)} - \frac{M_b}{\delta}\cos\left(\tfrac{1}{2}\pi r^2\right)\frac{\partial \tilde{u}_r^{(1)}}{\partial \zeta} + \frac{\partial^2 \tilde{u}_r^{(1)}}{\partial \zeta^2} = \frac{1}{\gamma}\frac{\partial \tilde{p}^{(1)}}{\partial r} + \frac{\partial^2 \tilde{u}_\zeta^{(0)}}{\partial r \partial \zeta} \tag{69}$$

$$ik_{mn}\tilde{u}_\theta^{(1)} - \frac{M_b}{\delta}\cos\left(\tfrac{1}{2}\pi r^2\right)\frac{\partial \tilde{u}_\theta^{(1)}}{\partial \zeta} + \frac{\partial^2 \tilde{u}_\theta^{(1)}}{\partial \zeta^2} = -\frac{1}{\gamma}\frac{1}{r}\frac{\partial \tilde{p}^{(1)}}{\partial \theta} + \frac{1}{r}\frac{\partial^2 \tilde{u}_\zeta^{(0)}}{\partial \theta \partial \zeta} \tag{70}$$

$$\frac{1}{\gamma}\frac{\partial \tilde{p}^{(1)}}{\partial \zeta} = ik_{mn}\tilde{u}_\zeta^{(0)} - \frac{M_b}{\delta}\cos\left(\tfrac{1}{2}\pi r^2\right)\frac{\partial \tilde{u}_\zeta^{(0)}}{\partial \zeta} \tag{71}$$

By virtue of $\tilde{u}_\zeta^{(0)} = 0$, Eq. (71) can be solved to obtain $\tilde{p}^{(1)} = 0$. The outcome may be substituted into Eq. (69) to arrive at a second-order homogeneous PDE in $\tilde{u}_r^{(1)}$, namely

$$ik_{mn}\tilde{u}_r^{(1)} - \frac{M_b}{\delta}\cos\left(\tfrac{1}{2}\pi r^2\right)\tfrac{\partial \tilde{u}_r^{(1)}}{\partial \zeta} + \tfrac{\partial^2 \tilde{u}_r^{(1)}}{\partial \zeta^2} = 0 \tag{72}$$

The physical solution of Eq. (72) mirrors its counterpart at leading order with

$$\tilde{u}_r^{(1)} = A_{r1}\left(t, r, \theta\right)e^{X_{1C}\zeta} \tag{73}$$

Consistently with the uniform flow case, it is possible to deduce that $\tilde{u}_r^{(1)} = \tilde{u}_\theta^{(1)} = 0$. Lastly, to extract the axial correction, Eqs. (66) and (67) may be inserted into Eq. (68) to retrieve

$$\begin{aligned}\frac{\partial \tilde{u}_\zeta^{(1)}}{\partial \zeta} = \frac{i}{\gamma k_{mn}} e^{-ik_{mn}t}\big[k_{mn}^2 J_m\big(k_{mn}r\big)e^{X_{1C}\zeta} \\ -\zeta e^{X_{1C}\zeta}X_{1C}' J_m'\big(K_{mn}r\big)\big]\cos(m\theta)\end{aligned} \tag{74}$$

Recalling that $\tilde{u}_\zeta^{(1)} = 0$ at the headwall, Eq. (74) may be integrated with respect to ζ and simplified into

$$\begin{aligned}\tilde{u}_\zeta^{(1)} = \frac{i}{k_{mn}\gamma}\frac{1}{X_{1C}} e^{-ik_{mn}t}\Big[k_{mn}^2 J_m(k_{mn}r)(e^{X_{1C}\zeta} - 1) \\ -\frac{X_{1C}'}{X_{1C}} J_m'(k_{mn}r)(\zeta e^{X_{1C}\zeta}X_{1C} + 1 - e^{X_{1C}\zeta})\Big]\cos(m\theta)\end{aligned} \tag{75}$$

Figure 3 showcases the unsteady velocity vectors in a chamber cross section taken at $t = 0.01$ s and an axial distance of $\zeta = 1$ from the headwall. The four parts correspond to the same representative cases and mode numbers used to describe the acoustic pressure in Fig. 2. As one would expect, the rich vorticoacoustic wave structures that emerge are strongly influenced by the acoustic mode shapes. The nodal lines appear to be at either 90 or 45 deg angles with respect to the pressure, thus leading to the horizontal (instead of vertical) symmetry in parts a) and b) where $m = 1$, and straight crosses (instead of oblique crosses) in parts c) and d) where $m = 2$. In comparison to the acoustic pressure distribution displayed in Fig. 2, the nodal lines of the vorticoacoustic waves are shifted by a phase angle of $\pi/(2m)$.

IV. Results and Discussion

The analytical approximations obtained heretofore can be collected into two sets of expressions for the vorticoacoustic velocity and pressure distributions. The significance of these results and the behavior of their corresponding waves will now be discussed. Furthermore, the wave behavior associated with each of the two mean flow profiles will be compared and contrasted.

To start, a summary of the vorticoacoustic wave components will be provided through the superposition of potential and rotational contributions. The resulting unsteady fluctuations are given by

$$\text{Uniform injection:}\quad \begin{cases} p' = e^{-ik_{mn}t}J_m(k_{mn}r)\cos(m\theta) + \mathcal{O}(M_b, \delta^2) \\ u_r' = \frac{i}{k_{mn}\gamma}e^{-ik_{mn}t}(k_{mn}r)\cos(m\theta)(e^{X_1\zeta}) + \mathcal{O}(M_b, \delta^2) \\ u_\theta' = \frac{i}{k_{mn}\gamma}\frac{m}{r}e^{-ik_{mn}t}J_m(k_{mn}r)\sin(m\theta)(1 - e^{X_1\zeta}) + \mathcal{O}(M_b, \delta^2) \\ u_z' = \frac{ik_{mn}}{\gamma}\frac{\delta}{X_1}e^{-ik_{mn}t}J_m(k_{mn}r)\cos(m\theta)(e^{X_1\zeta} - 1) + \mathcal{O}(\delta^3) \end{cases} \tag{76}$$

and

$$\text{Bell-shaped injection:}\quad \begin{cases} p' = e^{-ik_{mn}t}J_m(k_{mn}r)\cos(m\theta) + \mathcal{O}(M_b, \delta^2) \\ u_r' = \frac{i}{k_{mn}\gamma}e^{-ik_{mn}t}J_m'(k_{mn}r)\cos(m\theta)(e^{X_{1C1}\zeta} - 1) + \mathcal{O}(M_b, \delta^2) \\ u_\theta' = \frac{i}{k_{mn}\gamma}\frac{m}{r}e^{-ik_{mn}t}J_m(k_{mn}r)\sin(m\theta)(1 - e^{X_{1C}\zeta}) + \mathcal{O}(M_b, \delta^2) \\ u_z' = \frac{i}{k_{mn}\gamma}\frac{\delta}{X_{1C}}e^{-ik_{mn}t}\cos(m\theta)\begin{bmatrix} k_{mn}^2 J_m(k_{mn}r)(e^{X_{1C}\zeta} - 1) \\ -\frac{X_{1C}'}{X_{1C}}J_m'(k_{mn}r)(\zeta e^{X_{1C}\zeta}X_{1C} + 1 - e^{X_{1C}\zeta}) \end{bmatrix} + \mathcal{O}(\delta^3) \end{cases} \tag{77}$$

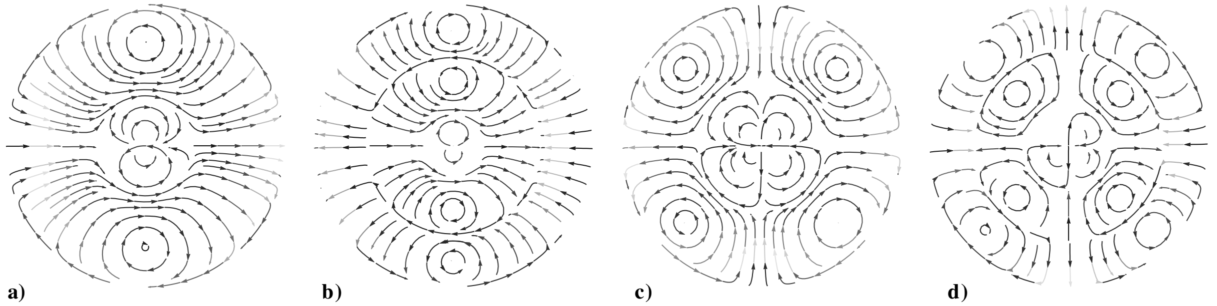

a) b) c) d)

Fig. 3 Vorticoacoustic velocity vectors in a polar slice taken at $\zeta = 1$ and transverse mode numbers corresponding to: a) $k_{11} = 5.3314$, b) $k_{12} = 8.5363$, c) $k_{21} = 6.7061$, and d) $k_{22} = 9.9695$.

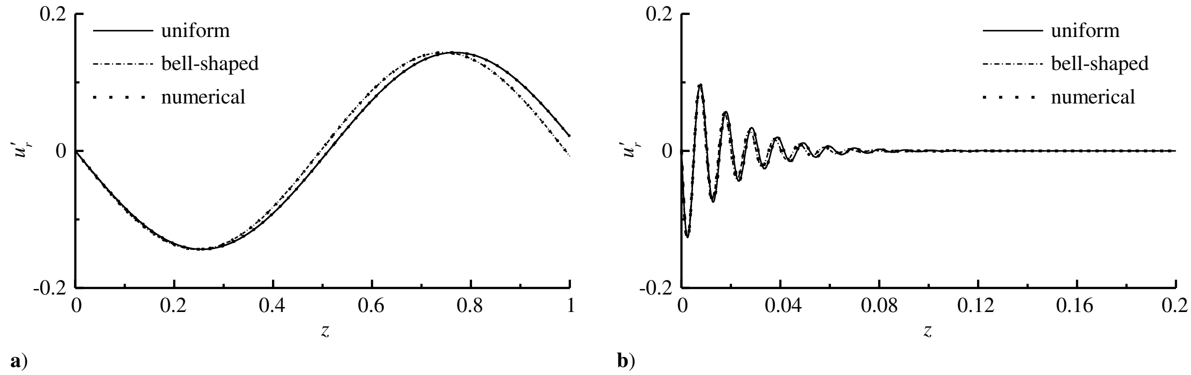

Fig. 4 Unsteady radial velocity at inlet Mach numbers corresponding to: a) 0.3 and b) 0.003.

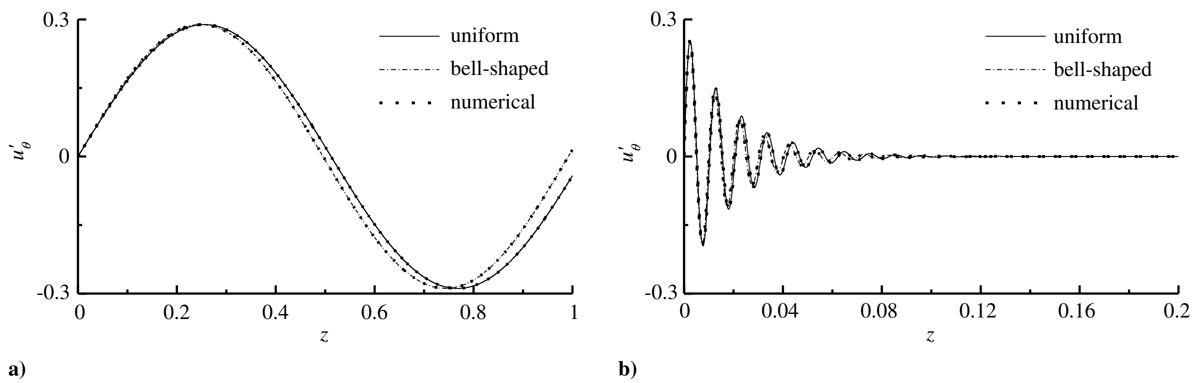

Fig. 5 Unsteady tangential velocity at inlet Mach numbers corresponding to: a) 0.3 and b) 0.003.

For the sake of illustration, Figs. 4–6 are used to display the behavior of the radial, tangential and axial disturbances versus the axial coordinate at decreasing values of the inlet Mach number. This is achieved at $t = 0$, $r = 0.4$, $\theta = \frac{1}{3}\pi$, $\delta = 0.000647$, and a thrust chamber with a unit aspect ratio ($L/R = 1$) [21]. The corresponding plots capture the oscillatory motion for the first tangential mode using k_{10}. Furthermore, Figs. 4–6 display the unsteady velocities at two inlet Mach numbers that differ by two orders of magnitude: $M_b =$ 0.3 and 0.003.

A. Numerical Verification

By way of verification, a numerical solver is written to compute the solutions corresponding to Eqs. (29–32), (42–45), (58–61), and (68–71). The solver uses a shooting scheme in conjunction with Mathematica's built-in numerical integrators to perform the necessary calculations. To ensure numerical stability and reduce interpolation errors, we find it essential to begin integrating at the end of the domain, where $z = 1$, and work our way back to the headwall.

In order to ensure conformity between the derived analytical solutions and their numerical counterparts, we evaluate the system of vortical equations for the cases described in the previous sections, i.e., for $t = 0$, $r = 0.4$, $\theta = \frac{1}{3}\pi$, $\delta = 0.000647$, the first tangential mode, and two Mach numbers that bracket the range of 0.003–0.3. The numerical results are shown using black dots in Figs. 4–6. Given that the level of agreement between numerics and asymptotics is quite favorable, we now proceed to characterize the vorticoacoustic waves based on the analytical solutions given by Eqs. (76) and (77).

B. Wave Characterization

It should be noted that the expressions for unsteady radial and tangential velocities in Eqs. (76) and (77) are nearly identical. The effect of specific mean flow motion is manifested through the axial constants X_1 and X_{1C}. Were it not for this mean flow dissimilarity, the two sets in the radial and tangential directions would have been identical. The corresponding spatial distributions are, hence, expected to behave similarly, with minor shifts that are caused by differences in their mean flow speeds. This observation is confirmed by the plots in Figs. 4–6. For example, at $r = 0.4$, the mean flow speed takes on a value of unity for the uniform flow and 0.9686 for the bell-shaped profile. This small difference may explain the slower downstream propagation of the unsteady traveling wave associated with the bell-shaped profile relative to the solution connected with the uniform mean flow.

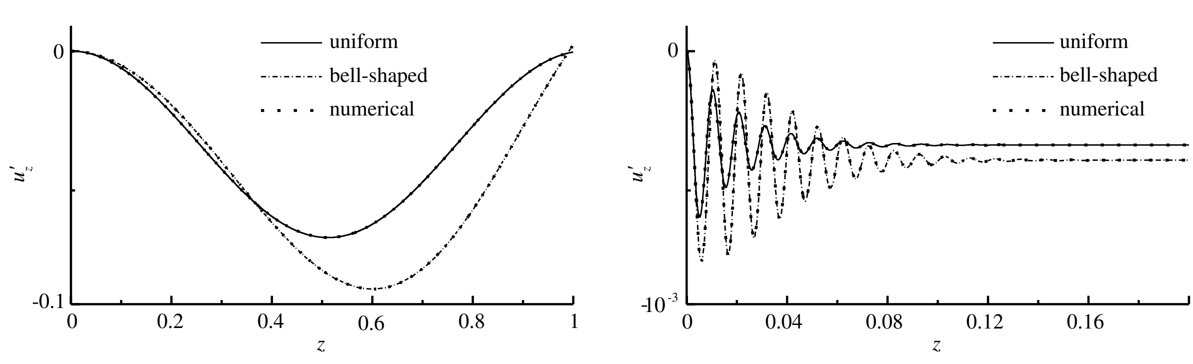

Fig. 6 Unsteady axial velocity at inlet Mach numbers corresponding to: a) 0.3 and b) 0.003.

Interestingly, an inspection of the asymptotic orders reveals that the radial and tangential vortical velocities appear at order δ^2 (hence, of order Re_a^{-1}). This is an important observation since, in classical fluid dynamics, the normalization and subsequent analysis are traditionally based on the reciprocal of the Reynolds number, a quantity that is often taken as the primary perturbation parameter in lieu of the viscous parameter, δ. In short, it can be shown that these two velocity corrections skip every odd order and, therefore, appear only at even powers of δ. Then one may argue whether their derivation could have been achieved using the more traditional expansion in the reciprocal of the Reynolds number. The answer is negative, and this is owed in large part to the behavior of $\tilde{u}_z$. Unlike $\tilde{u}_r$ and $\tilde{u}_\theta$, the expansion of the axial vortical velocity $\tilde{u}_z$ is shifted by an order of δ from its tangential and radial counterparts, as one may infer from Eqs. (76) and (77). This also justifies the strategy used in the present approach, including the coordinate transformation that requires stretching the axial coordinate using the viscous parameter in lieu of the inverted Reynolds number.

Concerning the vortical pseudopressure, it may be instructive to note that, although $\tilde{p}$ is not dismissed at the onset from the rotational momentum equation, it is carefully derived and shown to be strictly zero for the first two orders in δ. We can, therefore, project that the vortical wave will only affect the acoustic pressure distribution starting at order δ^2. This observation confirms the analogous treatment of the longitudinal wave problem in a simulated SRM, where the vortical pressure is discarded throughout the analysis [18,40]. Here, its dismissal is formally established.

Returning to the wave velocity, the behavior of the vortical component in the axial direction deserves particular attention. Recalling that the acoustic component of the axial wave is discounted here (assuming a short chamber), the unsteady axial wave, u_z', becomes confounded with the vortical part, $\tilde{u}_z$. The latter is needed to compensate for the more dominant tangential and radial components and, in the process, ensure that continuity is firmly satisfied.

Figure 6 illustrates the behavior of u_z' for two injection Mach numbers. In these snapshots, the average unsteady velocity appears to be negative in the uniform injection case. Although the same average for the bell-shaped profile proves to be negative at this chamber location, its magnitude exhibits a smaller absolute value. The resulting behavior may be elucidated by turning our attention to the source of the axial solution. Given that the asymptotically reduced form of the continuity equation stands at the basis of u_z', the actual determination of the axial fluctuation remains intertwined with the behavior of the transverse wave gradients at any prescribed location. The negative oscillations in the axial direction are, therefore, required to locally satisfy continuity. Regarding the speed of the mean flow at $r = 0.4$, the bell-shaped pattern, in comparison to the uniform motion, possesses less energy to sustain the traveling wave motion. This explains why its propagation is accompanied by faster attenuation.

To further explore this point, an inspection of the axial constant X_{1C} in Eq. (63) confirms that, at the centerline, the bell-shaped pattern yields a value of unity, which matches the uniform flow case. Moreover, as we move away toward the sidewall, the cosine function approaches zero. In close proximity of the sidewall, the axial constant tends to negative infinity, having a negative real part. It may, therefore, be seen that at the sidewall, Eq. (77) reduces to

$$\begin{cases} p' = e^{-ik_{mn}t} J_m(k_{mn}r)\cos(m\theta) + \mathcal{O}(M_b, \delta^2) \\ u_r' = 0 + \mathcal{O}(M_b, \delta^2) \\ u_\theta' = \frac{im}{k_{mn}\gamma} e^{-ik_{mn}t} J_m(k_{mn})\sin(m\theta) + \mathcal{O}(M_b, \delta^2) \\ u_z' \approx 0 + \mathcal{O}(\delta^3) \end{cases} \tag{78}$$

Equation (78) shows that through the use of a bell-shaped mean flow, the ensuing transverse wave motion can intrinsically satisfy the no-slip requirement, not only at the headwall, but at the sidewall as well. This is true for the dominant component of the wave u_r', while being asymptotically correct for the axial component u_z'. As for the contribution of the tangential component u_θ' its value at the sidewall mirrors that of the acoustic component because the vortical contribution vanishes locally. It may hence be argued that the ability of this model to satisfy the physical requirements along all boundaries grants it more generality than its predecessor with uniform headwall injection.

C. Penetration Number and Rotational Layer Thickness

Figures 4–6 illustrate the dependence of the wave's boundary-layer thickness on the injection Mach number. It is apparent that the viscous forces dominate over the inertial forces as the injection Mach number is reduced. Conversely, when the injection Mach number is increased, the boundary layer is blown off the headwall [41]. It may be noted that the faster decay of the wave (caused by a lower Mach number) results in a lower propagation wavelength as measured by the peak-to-peak distance.

Physically, the behavior of the propagation wavelength may be attributed to the wave's Strouhal number, or dimensionless frequency, defined by $S = k_{mn}/M_b$. A decrement in the injection Mach number and its corresponding increment in the Strouhal number lead to a larger number of reversals per unit time. Furthermore, the increased frequency results in a higher interaction rate between fluid particles, and the increased friction between shear layers leads to a more rapid attenuation of the wave amplitude.

Algebraically, the same behavior may be deduced by rewriting the axial decay terms X_1 and X_{1C} of Eqs. (35) and (63) in terms of the Strouhal number and another dimensionless parameter. To this end, two-term Maclaurin series approximations of X_1 and X_{1C} are required to capture the wave amplitude and propagation parameters. These are

$$X_1 \approx i\frac{k_{mn}\delta}{M_b} - \frac{k_{mn}^2\delta^3}{M_b^3} = \delta\left(iS - \frac{1}{S_p}\right) \tag{79}$$

and

$$\begin{aligned} X_{1C} &\approx i\frac{k_{mn}\delta}{M_b\cos\left(\frac{1}{2}\pi r^2\right)} - \frac{k_{mn}^2\delta^3}{M_b^3\cos^3\left(\frac{1}{2}\pi r^2\right)} \\ &= \delta\left[iS\sec\left(\tfrac{1}{2}\pi r^2\right) - \frac{\sec^3\left(\frac{1}{2}\pi r^2\right)}{S_p}\right] \end{aligned} \tag{80}$$

where the effective penetration number S_p emerges in the form

$$S_p = \frac{M_b^3}{k_{mn}^2\delta^2} = \left(\frac{U_b^3}{a_0^3}\right)\left(\frac{a_0 R}{\nu_0}\right)\left(\frac{a_0^2}{\omega_0^2 R^2}\right) = \frac{U_b^3}{\nu_0\omega_0^2 R} \tag{81}$$

This parameter, first discovered by Majdalani in 1992 and discussed by [25], plays a key role in the characterization of the boundary-layer thickness of the longitudinal vorticoacoustic wave in a simulated SRM. Note that an increase in S_p leads to a deeper penetration of the wave. From a physical standpoint, the penetration number gauges the balance between two basic forces: unsteady inertia and viscous diffusion of the radial and tangential velocities in the axial direction. For the radial velocity, S_p may be viewed as the ratio of

$$\begin{aligned} \frac{\text{unsteady inertial force}}{\text{viscous force}} &\approx \frac{\frac{\partial u_r^*}{\partial t^*}}{\nu\frac{\partial^2 u_r^*}{\partial z^{*2}}} \approx \frac{\frac{u_r^*}{t^*}}{\nu\frac{u_r^*}{z^{*2}}} = \frac{z^{*2}}{\nu t^*} \\ &\approx \frac{(U_b/\omega_0)^2}{\nu(R/U_b)} = \frac{U_b^3}{\nu_0\omega_0^2 R} = S_p \end{aligned} \tag{82}$$

In the present study, the wave expressions may be recast using the Strouhal and penetration numbers. For the bell-shaped injection profile, the (real) magnitudes of the waves in Eq. (77) are governed by

$$u_r' \sim J_m'(k_{mn}r)\left[1 - \exp\left(-\frac{z}{S_p\cos^3\eta}\right)\right] \tag{83}$$

$$u_\theta' \sim J_m(k_{mn}r)\left[1 - \exp\left(-\frac{z}{S_p\cos^3\eta}\right)\right] \tag{84}$$

and

$$u_z' \sim S_p \cos^3\eta \left\{ \begin{array}{l} k_{mn}^2 J_m(k_{mn}r)\left[\exp\left(-\frac{z}{S_p \cos^3\eta}\right) - 1\right] \\ -\pi r \tan\eta J_m'(k_{mn}r)\left[\frac{z}{S_p \cos^3\eta}\exp\left(-\frac{z}{S_p \cos^3\eta}\right) - \exp\left(-\frac{z}{S_p \cos^3\eta}\right) + 1\right] \end{array} \right\} \tag{85}$$

where $\eta \equiv \frac{1}{2}\pi r^2$.

An inspection of Eqs. (83–85) reveals that, at the sidewall, the radial and axial components vanish, while the tangential component scales with $J_m(k_{mn})$; this behavior is consistent with the observations of the previous section. The rotational boundary layer can also be deduced from Eqs. (83) and (84). The penetration of rotational elements is traditionally defined as the distance from the injecting wall to the point where the contribution of the vortical wave becomes negligible, traditionally taken at 1% of the acoustic wave [41]. Because the axial component of the potential field vanishes in the farfield, the penetration depth may be deduced for the radial and tangential components by putting

$$\exp\left(-\frac{z}{S_p \cos^3\eta}\right) = \alpha \equiv 0.01 \tag{86}$$

where α corresponds to 1% and z_p denotes the axial thickness of the rotational boundary layer. Rearranging Eq. (86) renders

$$z_p = S_p \cos^3\left(\frac{1}{2}\pi r^2\right)\ln(\alpha^{-1}) = \frac{M_b^3}{k_{mn}^2\delta^2}\cos^3\left(\frac{1}{2}\pi r^2\right)\ln(\alpha^{-1}) \tag{87}$$

Figure 7 correlates the thickness of the vorticoacoustic boundary layer to the injection Mach number and viscous parameter. In conjunction with the expression in Eq. (87), Fig. 7 shows that the boundary layer is thick for large injection Mach numbers, exceeding by far the length of the chamber. When this case occurs, the linear oscillations have no time to decay before exiting the chamber. On the other hand, in the case of a small injection Mach number, the oscillations would take their toll almost entirely in the injector zone before fading out elsewhere. Moreover, the particular dependence on the injection pattern may be inferred from the expression of the penetration depth. The boundary-layer thickness reaches its peak at the centerline, where disturbances are convected into the chamber at the largest headwall velocity and then depreciates precipitously to zero at the sidewall where the mean flow is forced to rest.

Figure 8 compares the rotational boundary layers in the axial (SRM) and transverse (LRE) cases along with their dependence on the penetration number. In a simulated SRM, particles injected radially at the sidewall must turn before merging in the longitudinal direction, parallel to the chamber axis. This causes the penetration depth to increase in the direction along which unsteady vorticity is swept by virtue of the mean flow. Conversely, in a simulated LRE, injection takes place at the headwall and remains unaffected by the downstream convection of unsteady vorticity. The thickness of the boundary layer is, thus, dependent only on the speed of injection. Throughout the chamber, a linear correlation, given by Eq. (87), controls the depth of penetration. Unlike the axially dominated wave problem for which the wall-normal depth of penetration y_p approaches a maximum inviscid upper limit as $S_p \to \infty$, the axial depth of penetration, z_p, continues to grow linearly with S_p until the physical limitations of the model are exceeded. This behavior is also captured in Figs. 4 and 5 where the sweeping motion of vorticoacoustic waves over the entire chamber volume is accompanied by

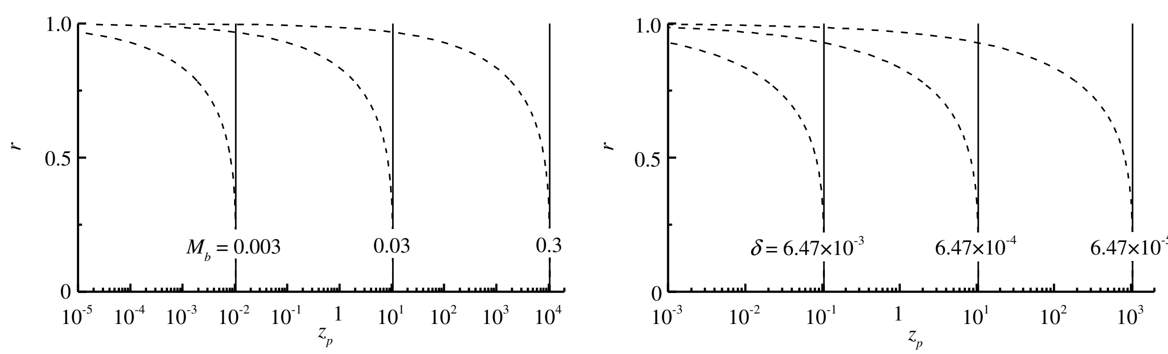

a) b)

Fig. 7 Different penetration depths at: a) $\delta = 0.000647$ and b) $M_b = 0.03$. Solid and dashed lines refer to the uniform and bell-shaped profiles, respectively.

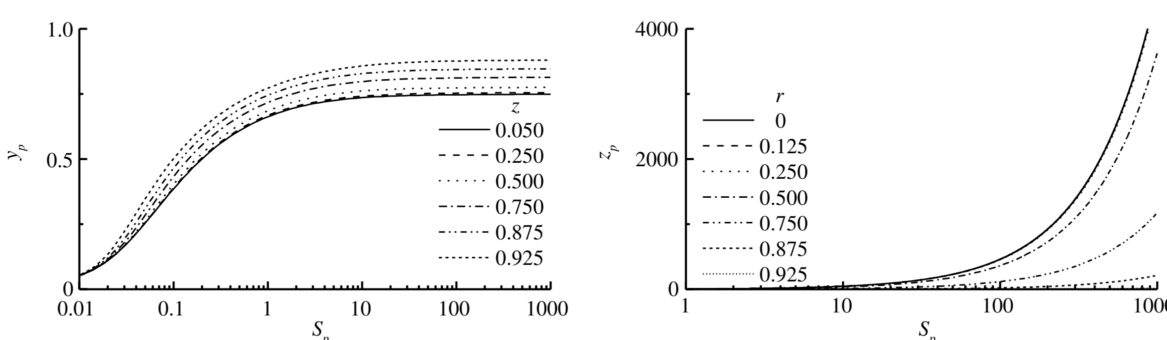

a) b)

Fig. 8 Penetration depth of the vortical wave corresponding to: a) axial [41] and b) transverse configurations.

no discernible attenuation for the case of $M_b = 0.3$. In contrast, Figs. 4 and 5 confirm that the wave decay in the vicinity of the headwall is much more pronounced for a reduced value of $M_b = 0.003$.

D. Wave Properties

In addition to the penetration depth, three properties must be investigated to complete our characterization of the vorticoacoustic wave behavior. These consist of the spatial wavelength, λ, the unsteady velocity overshoot factor, OF, and its spatial locus, z_{OS}. Granted that the radial and tangential components have nearly identical expressions, the following analysis is performed using the radial component only. Nonetheless, the upcoming procedure is applicable to both waves.

1. Spatial Wavelength

The spatial wavelength, λ, refers to the distance traveled by a wave during one period. It also denotes the distance between two consecutive peaks. To calculate λ, the wave propagation speed in the axial direction must be determined. To this end, the radial component of the vortical wave in Eq. (77) can be first rewritten as

$$\tilde{u}_r = F(r,\theta,z)\exp\left\{i\left[S\sec\left(\tfrac{1}{2}\pi r^2\right)z - k_{mn}t\right]\right\} \tag{88}$$

where F represents the amplitude of the wave. With the propagation of the wave in the axial direction being our primary concern, differentiation of the axial component is required to find the corresponding velocity. We have

$$S\sec\left(\tfrac{1}{2}\pi r^2\right)\mathrm{d}z - k_{mn}\,\mathrm{d}t = 0 \quad \text{or} \quad V_w = \frac{\mathrm{d}z}{\mathrm{d}t} = \frac{k_{mn}\cos\left(\frac{1}{2}\pi r^2\right)}{S} = M_b\cos\left(\tfrac{1}{2}\pi r^2\right) \tag{89}$$

Knowing that the period of oscillation is $\tau = 2\pi/k_{mn}$, the spatial wavelength is retrieved as

$$\lambda_s = V_w\tau = \frac{\cos\left(\frac{1}{2}\pi r^2\right)}{S} \tag{90}$$

Consistent with the classic theory of periodic flows [42], we note that the velocity of propagation is dependent only on the medium and conditions, i.e., the injection Mach number and the radial distance from the centerline. Moreover, the wavelength depends on the mode number, which is embedded in the Strouhal number. Higher modes reduce the peak-to-peak distance between oscillations, as one would expect. An important characteristic of this model is the dependence of all properties on the radial distance from the centerline. Accordingly, oscillations in the vicinity of the sidewall propagate at a much slower rate than those located near the chamber core.

2. Unsteady Velocity Overshoot

The presence of the Strouhal number in the argument of the vortical solution serves to control the phase difference between the strictly acoustic and vortical waves. Due to their phase difference, the two waves will periodically couple at nearly the same phase, thus, resulting in an overshoot of the unsteady velocity that can reach, in some cases, twice the acoustic wave amplitude. This type of overshoot was first reported by Richardson [43], and then Richardson and Tyler [44], before becoming known officially as the 'Richardson's annular effect.' In the corresponding classical experiments, Richardson originally anticipated that the maximum axial velocity measurements would occur near the centerline of his resonator tubes, as would be expected of viscous flows in circular cylinders. Instead, the largest amplitudes were detected in the vicinity of the sidewall, a behavior that was deemed unusual at first. Upon further scrutiny, the observed velocity amplifications were attributed to the phase shift that existed between the main acoustic oscillations and viscous-generated rotational waves at the wall. In the case of transverse waves in LREs, it is essential to evaluate whether such an overshoot can occur especially that it stands to increase the amplitude of the vorticoacoustic waves near the headwall. Naturally, more severe damage to the injector faceplates can be induced as a result of this potential doubling in acoustic wave amplitude.

Knowing that the overshoot takes place when both waves travel in phase, this condition may be recreated according to Eq. (88) when

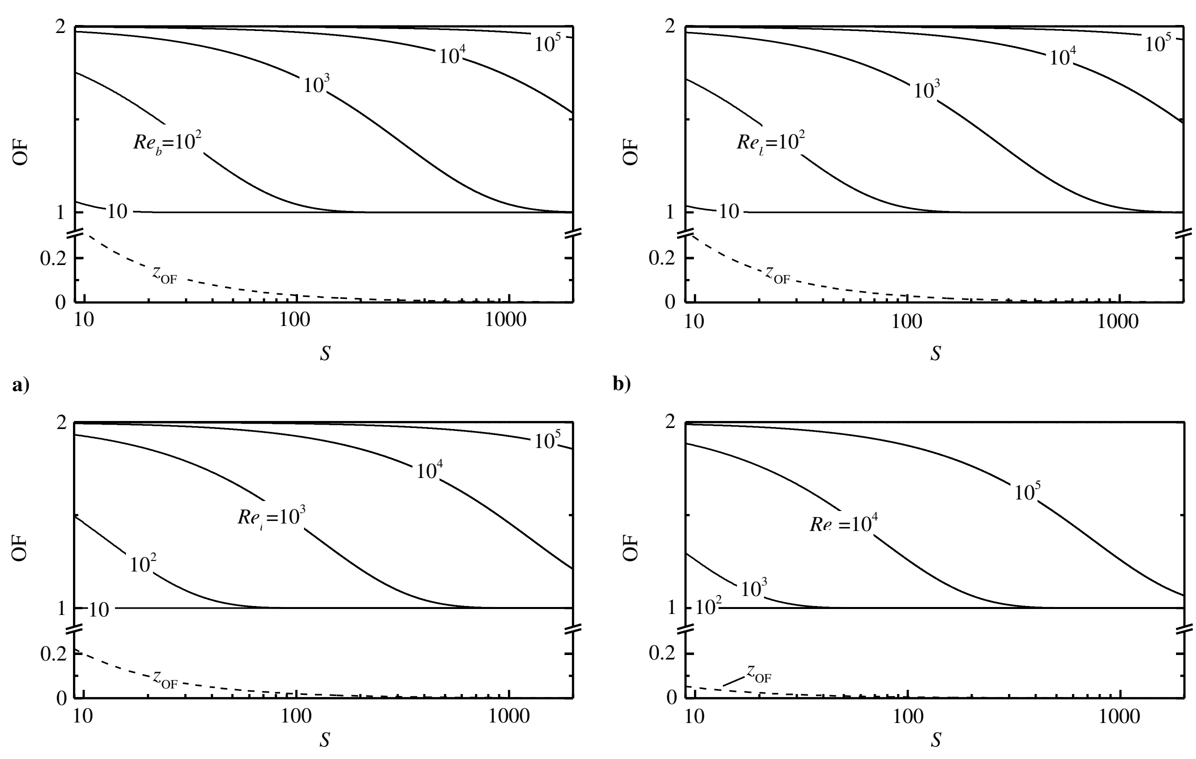

Fig. 9 Overshoot factor and locus of overshoot at: a) $r = 0$, b) $r = 0.05$, c) $r = 0.75$, and d) $r = 0.95$.

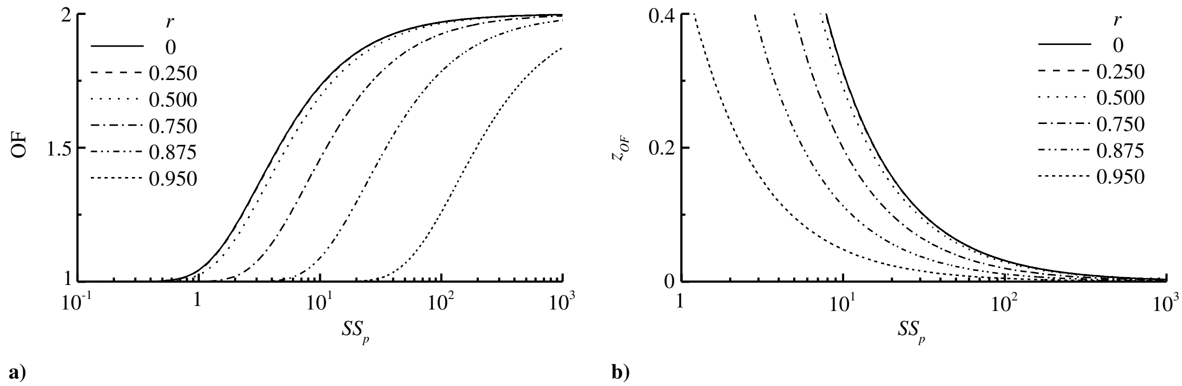

Fig. 10 Effect of radial distance on: a) the wave overshoot factor and b) its locus.

$\tilde{u}_r = -F(r,\theta,z)\exp(-ik_{mn}t)$; the locus of the overshoot can thus be deduced to be

$$z_{\mathrm{OS}} = \frac{\pi}{S}\cos\left(\tfrac{1}{2}\pi r^2\right) \tag{91}$$

Given our underlying normalization, the induced overshoot factor can be determined by combining the axial contribution of the vortical correction to that of the acoustic wave. The overshoot factor OF can be extracted from Eq. (77) and (80) by evaluating the amplitude of the vorticoacoustic velocity at $z = z_{\mathrm{OS}}$. Starting with

$$\mathrm{OF} = 1 - \exp\left[iS\sec\left(\tfrac{1}{2}\pi r^2\right)z_{\mathrm{OS}} - \frac{\sec^3(\frac{1}{2}\pi r^2)}{S_p}z_{\mathrm{OS}}\right] \tag{92}$$

we have

$$\mathrm{OF} = 1 + \exp\left[-\frac{\pi}{\cos^2(\frac{1}{2}\pi r^2)}\frac{S}{Re_b}\right] = 1 + \exp\left[-\frac{\pi}{\cos^2(\frac{1}{2}\pi r^2)}\frac{1}{SS_p}\right] \tag{93}$$

Figure 9 quantifies the overshoot factor and its locus for different control parameters. Note that on one hand, OF depends on the Strouhal number, the distance from the centerline, and the average chamber viscosity; the latter is accounted for through the blowing Reynolds number at the headwall, $Re_b = M_b Re_a = U_b R/\nu_0$. On the other hand, the different figures and their families of curves collapse into single lines (depicted in Fig. 10a) when plotted versus the product of the Strouhal and penetration numbers. Figure 10a shows that the strength of the overshoot decreases as we move away from the chamber centerline and increases at higher values of SS_p, i.e., with larger injection velocities or smaller frequencies. However, the locus of the overshoot depends solely on the Strouhal number and the distance from the centerline. For practical values of the Strouhal number, the overshoot takes place in the neighborhood of the headwall within 25% of the chamber radius. Recalling that faceplate injectors protrude inwardly, they can be subjected to oscillations reaching twice the strength of the predicted acoustic waves, even in the linear range. Additionally, it appears that the distance from the centerline affects the overshoot and its properties. The slower injection rate near the sidewalls leads to a smaller overshoot factor. Furthermore, as one may infer from Eq. (91) and Fig. 10b, z_{OS} diminishes away from the centerline and vanishes along the sidewall. This behavior shifts the line of maximum wave amplitude closer to the headwall as the sidewall is approached. In the case of a liquid rocket engine, these spatial excursions of peak transverse amplitudes serve to amplify shearing stresses on the injectors, where coupling between modes can lead to further steepening and shock-like behavior.

V. Conclusions

In this study, asymptotic expansion tools are used to capture small-to-moderate amplitude oscillations that are dominated by their transverse motion in a short circular cylinder that mimics the cold flow environment of a simple liquid rocket engine. Two particular formulations are advanced, and these correspond to either uniform or bell-shaped cosine-like injection patterns at the chamber headwall. After decomposing the unsteady wave into potential and rotational fields, the latter is resolved using a boundary-layer formulation that relies on a small viscous parameter, δ. This parameter corresponds to the square root of the inverted Reynolds number based on viscosity and the speed of sound. At the outset, several fundamental flow features are unraveled including the radial, tangential, and axial velocities of the time-dependent vortical field. For example, the pseudopressure associated with the rotational motion is rigorously derived and shown to be immaterial to the present analysis. The penetration number, a keystone parameter that controls the depth of penetration of unsteady vorticity, is also identified. It is seen to be nearly identical to its counterpart arising in the longitudinal wave analog encountered in the treatment of oscillatory motion in solid rocket motors (SRMs). The advent of this parameter enables the full characterization of the depth of penetration in the direction normal to the injecting surface. Furthermore, the formulation for the unsteady motion connected with uniform headwall injection is found to be consistent with a previous study aimed at investigating acoustic streaming in a cylindrical cavity. The zeroth-order injection model, however, leads to a transverse wave solution that allows slip along the sidewall. An improved formulation is presented here based on a bell-shaped injection profile. The latter is shown to satisfy the no-slip boundary at both headwall and chamber sidewall for the radial and axial components.

With the vorticoacoustic solution at hand, fundamental wave propagation properties are carefully extracted and discussed. These include the depth of penetration and Richardson's overshoot factor of the transverse waves. These are found to be strongly dependent on the Strouhal and penetration numbers. The latter represents a keystone parameter that seems to recur whenever oscillatory wave motion is considered above an injecting surface. The locus of peak wave amplitude, in particular, is found to be smaller than a quarter radius, thus placing the maximum shearing stresses (resulting from transverse wave motion) in the close vicinity of the headwall. In future work, the steepening of these waves will be examined. It is also hoped that a similar mathematical strategy will be later pursued to achieve more general and higher order models of multidimensional waves in various geometric settings.

Acknowledgments

This material is based on work supported partly by the National Science Foundation and partly by the University of Tennessee Space Institute through institutional cost sharing.

References

[1] Richecoeur, F., Ducruix, S., Scouflaire, P., and Candel, S., "Experimental Investigation of High-Frequency Combustion Instabilities in Liquid Rocket Engine," *Acta Astronautica*, Vol. 62, No. 1, 2008, pp. 18–27.
doi:10.1016/j.actaastro.2006.12.034

[2] Clayton, R. M., "Experimental Measurements on Rotating Detonation-Like Combustion," JPL 32-788, Pasadena, CA, Aug. 1965.

[3] Clayton, R. M., Rogero, R. S., and Sotter, J. G., "An Experimental Description of Destructive Liquid Rocket Resonant Combustion," *AIAA Journal*, Vol. 6, No. 7, 1968, pp. 1252–1259.
doi:10.2514/3.4730

[4] Sotter, J. G., Woodward, J. W., and Clayton, R. M., "Injector Response to Strong High-Frequency Pressure Oscillations," *Journal of Spacecraft and Rockets*, Vol. 6, No. 4, 1969, pp. 504–506.
doi:10.2514/3.29696

[5] Smith, R., Ellis, M., Xia, G., Sankaran, V., Anderson, W., and Merkle, C. L., "Computational Investigation of Acoustics and Instabilities in a Longitudinal-Mode Rocket Combustor," *AIAA Journal*, Vol. 46, No. 11, 2008, pp. 2659–2673.
doi:10.2514/1.28125

[6] Ando, D., Inaba, K., and Yamamoto, M., "Numerical Investigation on the Transverse Wave Property of Two-Dimensional H_2-O_2-Diluent Detonations," AIAA Paper 2007-989, Jan. 2007.

[7] Chandrasekhar, S., and Chakravarthy, S., "Response of Non-Premixed Ducted Flame to Transverse Oscillations and Longitudinal Acoustic Coupling," AIAA Paper 2007-5655, July 2007.

[8] Vuillot, F., and Avalon, G., "Acoustic Boundary Layers in Large Solid Propellant Rocket Motors Using Navier-Stokes Equations," *Journal of Propulsion and Power*, Vol. 7, No. 2, 1991, pp. 231–239.
doi:10.2514/3.23316

[9] Fischbach, S. R., and Majdalani, J., "Volume-to-Surface Reduction of Vorticoacoustic Stability Integrals," *Journal of Sound and Vibration*, Vol. 321, Nos. 3–5, 2009, pp. 1007–1025.
doi:10.1016/j.jsv.2008.10.001

[10] Culick, F. E. C., "Acoustic Oscillations in Solid Propellant Rocket Chambers," *Acta Astronautica*, Vol. 12, No. 2, 1966, pp. 113–126.

[11] Culick, F. E. C., "High Frequency Oscillations in Liquid Rockets," *AIAA Journal*, Vol. 1, No. 5, 1963, pp. 1097–1104.

[12] Maslen, S. H., and Moore, F. K., "On Strong Transverse Waves without Shocks in a Circular Cylinder," *Journal of the Aeronautical Sciences*, Vol. 23, No. 6, 1956, pp. 583–593.

[13] Crocco, L., Harrje, D., and Reardon, F., "Transverse Combustion Instability in Liquid Propellant Rocket Motors," *Journal of the American Rocket Society*, Vol. 32, 1962, p. 366.

[14] Flandro, G. A., Majdalani, J., and Sims, J. D., "Nonlinear Longitudinal Mode Instability in Liquid Propellant Rocket Engine Preburners," AIAA Paper 2004-4162, July 2004.

[15] Flandro, G. A., Majdalani, J., and Sims, J. D., "On Nonlinear Combustion Instability in Liquid Propellant Rocket Engines," AIAA Paper 2004-3516, July 2004.

[16] Hart, R. W., and McClure, F. T., "Combustion Instability: Acoustic Interaction with a Burning Propellant Surface," *The Journal of Chemical Physics*, Vol. 30, No. 6, 1959, pp. 1501–1514.
doi:10.1063/1.1730226

[17] Hart, R. W., and McClure, F. T., "Theory of Acoustic Instability in Solid-Propellant Rocket Combustion," *Tenth Symposium (International) on Combustion*, Vol. 10, No. 1, 1965, pp. 1047–1065.
doi:10.1016/S0082-0784(65)80246-6

[18] Majdalani, J., and Roh, T. S., "The Oscillatory Channel Flow with Large Wall Injection," *Proceedings of the Royal Society of London, Series A*, Vol. 456, No. 1999, 2000, pp. 1625–1657.
doi:10.1098/rspa.2000.0579

[19] Fabignon, Y., Dupays, J., Avalon, G., Vuillot, F., Lupoglazoff, N., Casalis, G., and Prévost, M., "Instabilities and Pressure Oscillations in Solid Rocket Motors," *Journal of Aerospace Science and Technology*, Vol. 7, No. 3, 2003, pp. 191–200.
doi:10.1016/S1270-9638(02)01194-X

[20] Fischbach, S. R., Majdalani, J., and Flandro, G. A., "Acoustic Instability of the Slab Rocket Motor," *Journal of Propulsion and Power*, Vol. 23, No. 1, 2007, pp. 146–157.
doi:10.2514/1.14794

[21] Fischbach, S., Flandro, G., and Majdalani, J., "Acoustic Streaming in Simplified Liquid Rocket Engines with Transverse Mode Oscillations," *Physics of Fluids*, Vol. 22, No. 6, 2010, pp. 063602–063621.
doi:10.1063/1.3407663

[22] Culick, F. E. C., "Rotational Axisymmetric Mean Flow and Damping of Acoustic Waves in a Solid Propellant Rocket," *AIAA Journal*, Vol. 4, No. 8, 1966, pp. 1462–1464.
doi:10.2514/3.3709

[23] Brown, R. S., Blackner, A. M., Willoughby, P. G., and Dunlap, R., "Coupling Between Acoustic Velocity Oscillations and Solid Propellant Combustion," *Journal of Propulsion and Power*, Vol. 2, No. 5, 1986, pp. 428–437.
doi:10.2514/3.22925

[24] Dunlap, R., Blackner, A. M., Waugh, R. C., Brown, R. S., and Willoughby, P. G., "Internal Flow Field Studies in a Simulated Cylindrical Port Rocket Chamber," *Journal of Propulsion and Power*, Vol. 6, No. 6, 1990, pp. 690–704.
doi:10.2514/3.23274

[25] Majdalani, J., and Van Moorhem, W. K., "A Multiple-Scales Solution to the Acoustic Boundary Layer in Solid Rocket Motors," *Journal of Propulsion and Power*, Vol. 13, No. 2, 1997, pp. 186–193.
doi:10.2514/2.5168

[26] Majdalani, J., and Van Moorhem, W., "Improved Time-Dependent Flowfield Solution for Solid Rocket Motors," *AIAA Journal*, Vol. 36, No. 2, 1998, pp. 241–248.
doi:10.2514/2.7507

[27] Majdalani, J., and Flandro, G. A., "The Oscillatory Pipe Flow with Arbitrary Wall Injection," *Proceedings of the Royal Society of London, Series A*, Vol. 458, No. 2023, 2002, pp. 1621–1651.
doi:10.1098/rspa.2001.0930

[28] Chedevergne, F., Casalis, G., and Majdalani, J., "Direct Numerical Simulation and Biglobal Stability Investigations of the Gaseous Motion in Solid Rocket Motors," *Journal of Fluid Mechanics*, Vol. 706, 2012, pp. 190–218.
doi:10.1017/jfm.2012.245

[29] Zinn, B. T., and Savell, C. T., "A Theoretical Study of Three-Dimensional Combustion Instability in Liquid-Propellant Rocket Engines," *Symposium (International) on Combustion*, Vol. 12, No. 1, 1969, pp. 139–147.
doi:10.1016/S0082-0784(69)80398-X

[30] Chu, B.-T., and Kovásznay, L. S. G., "Non-Linear Interactions in a Viscous Heat-Conducting Compressible Gas," *Journal of Fluid Mechanics*, Vol. 3, No. 5, 1958, pp. 494–514.
doi:10.1017/S0022112058000148

[31] Sutton, G. P., and Biblarz, O., *Rocket Propulsion Elements*, 7th ed., Wiley, New York, 2001, pp. 343–346.

[32] Berman, A. S., "Laminar Flow in Channels with Porous Walls," *Journal of Applied Physics*, Vol. 24, No. 9, 1953, pp. 1232–1235.
doi:10.1063/1.1721476

[33] Proudman, I., "An Example of Steady Laminar Flow at Large Reynolds Number," *Journal of Fluid Mechanics*, Vol. 9, No. 4, 1960, pp. 593–602.
doi:10.1017/S002211206000133X

[34] Beddini, R. A., "Injection-Induced Flows in Porous-Walled Ducts," *AIAA Journal*, Vol. 24, No. 11, 1986, pp. 1766–1773.
doi:10.2514/3.9522

[35] Chedevergne, F., Casalis, G., and Féraille, T., "Biglobal Linear Stability Analysis of the Flow Induced by Wall Injection," *Physics of Fluids*, Vol. 18, No. 1, 2006, pp. 014103–14.
doi:10.1063/1.2160524

[36] Griffond, J., and Casalis, G., "On the Nonparallel Stability of the Injection Induced Two-Dimensional Taylor Flow," *Physics of Fluids*, Vol. 13, No. 6, 2001, pp. 1635–1644.
doi:10.1063/1.1367869

[37] Majdalani, J., and Saad, T., "The Taylor-Culick Profile with Arbitrary Headwall Injection," *Physics of Fluids*, Vol. 19, No. 9, 2007, pp. 093601–10.
doi:10.1063/1.2746003

[38] Majdalani, J., "Analytical Models for Hybrid Rockets," *Fundamentals of Hybrid Rocket Combustion and Propulsion*, edited by Kuo, K., and Chiaverini, M. J., AIAA Progress in Astronautics and Aeronautics, Washington, D.C., 2007, pp. 207–246.

[39] Carrier, B. T., and Carlson, F. D., "On the Propagation of Small Disturbances in a Moving Compressible Fluid," *Quarterly of Applied Mathematics*, Vol. 4, No. 1, 1946, pp. 1–12.

[40] Majdalani, J., "Multiple Asymptotic Solutions for Axially Travelling Waves in Porous Channels," *Journal of Fluid Mechanics*, Vol. 636, No. 1, 2009, pp. 59–89.
doi:10.1017/S0022112009007939

[41] Majdalani, J., "The Boundary Layer Structure in Cylindrical Rocket Motors," *AIAA Journal*, Vol. 37, No. 4, 1999, pp. 505–508.
doi:10.2514/2.742

[42] Rott, N., "Theory of Time-Dependent Laminar Flows," *High Speed Aerodynamics and Jet Propulsion — Theory of Laminar Flows*, edited

by Moore, F. K., Vol. IV, Princeton Univ. Press, Princeton, NJ, 1964, pp. 395–438.

[43] Richardson, E., "The Amplitude of Sound Waves in Resonators," *Proceedings of the Physical Society, London*, Vol. 40, No. 27, 1928, pp. 206–220.
doi:10.1088/0959-5309/40/1/328

[44] Richardson, E., and Tyler, E., "The Transverse Velocity Gradient near the Mouths of Pipes in Which an Alternating or Continuous Flow of Air Is Established," *Proceedings of the Physical Society, London*, Vol. 42, No. 1, 1929, pp. 1–15.
doi:10.1088/0959-5309/42/1/302

T. Jackson
Associate Editor